



**HAL**  
open science

# An Absolute Calibration of the Near-infrared Period–Luminosity Relations of Type II Cepheids in the Milky Way and in the Large Magellanic Cloud

Piotr Wielgórski, Grzegorz Pietrzyński, Bogumil Pilecki, Wolfgang Gieren,  
Bartłomiej Zgirski, Marek Górski, Gergely Hajdu, Weronika Narloch, Paulina  
Karczmarek, Radosław Smolec, et al.

## ► To cite this version:

Piotr Wielgórski, Grzegorz Pietrzyński, Bogumil Pilecki, Wolfgang Gieren, Bartłomiej Zgirski, et al..  
An Absolute Calibration of the Near-infrared Period–Luminosity Relations of Type II Cepheids in  
the Milky Way and in the Large Magellanic Cloud. *The Astrophysical Journal*, 2022, 927 (1), pp.89.  
10.3847/1538-4357/ac470c . hal-03667347

**HAL Id: hal-03667347**

**<https://u-paris.hal.science/hal-03667347>**

Submitted on 13 May 2022

**HAL** is a multi-disciplinary open access archive for the deposit and dissemination of scientific research documents, whether they are published or not. The documents may come from teaching and research institutions in France or abroad, or from public or private research centers.

L'archive ouverte pluridisciplinaire **HAL**, est destinée au dépôt et à la diffusion de documents scientifiques de niveau recherche, publiés ou non, émanant des établissements d'enseignement et de recherche français ou étrangers, des laboratoires publics ou privés.



Distributed under a Creative Commons Attribution 4.0 International License



# An Absolute Calibration of the Near-infrared Period–Luminosity Relations of Type II Cepheids in the Milky Way and in the Large Magellanic Cloud

Piotr Wielgórski<sup>1</sup> , Grzegorz Pietrzyński<sup>1,2</sup> , Bogumił Pilecki<sup>1</sup> , Wolfgang Gieren<sup>2</sup> , Bartłomiej Zgirski<sup>1</sup> , Marek Górski<sup>1</sup> , Gergely Hajdu<sup>1</sup> , Weronika Narloch<sup>2</sup> , Paulina Karczmarek<sup>2</sup> , Radosław Smolec<sup>1</sup> , Pierre Kervella<sup>3</sup> , Jesper Storm<sup>4</sup> , Alexandre Gallenne<sup>2,5</sup> , Louise Breuval<sup>3,6</sup> , Megan Lewis<sup>1</sup> , Mikołaj Kałuszyński<sup>1</sup> , Dariusz Graczyk<sup>7</sup> , Wojciech Pych<sup>1</sup> , Ksenia Suchomska<sup>1</sup> , Mónica Taormina<sup>1</sup> , Gonzalo Rojas Garcia<sup>1</sup> , Aleksandra Kotek<sup>1</sup> , Rolf Chini<sup>1,8,9</sup> , Francisco Pozo Núñez<sup>8,10</sup> , Sadegh Noroozi<sup>8</sup> , Catalina Sobrino Figaredo<sup>8</sup> , Martin Haas<sup>8</sup> , Klaus Hodapp<sup>11</sup> , Przemysław Mikołajczyk<sup>12</sup> , Krzysztof Kotysz<sup>12</sup> , Dawid Moździerski<sup>12</sup> , and Piotr Kołaczek-Szymański<sup>12</sup>

<sup>1</sup>Nicolaus Copernicus Astronomical Center, Polish Academy of Sciences, Bartycka 18, 00-716 Warszawa, Poland; [pwielgor@camk.edu.pl](mailto:pwielgor@camk.edu.pl)

<sup>2</sup>Universidad de Concepción, Departamento de Astronomía, Casilla 160-C, Concepción, Chile

<sup>3</sup>LESIA, Observatoire de Paris, Université PSL, CNRS, Sorbonne Université, Université de Paris, 5 place Jules Janssen, F-92195 Meudon, France

<sup>4</sup>Leibniz-Institut für Astrophysik Potsdam (AIP), An der Sternwarte 16, D-14482 Potsdam, Germany

<sup>5</sup>Unidad Mixta Internacional Franco-Chilena de Astronomía (CNRS UMI 3386), Departamento de Astronomía, Universidad de Chile, Camino El Observatorio 1515, Las Condes, Santiago, Chile

<sup>6</sup>Department of Physics and Astronomy, Johns Hopkins University, Baltimore, MD 21218, USA

<sup>7</sup>Nicolaus Copernicus Astronomical Center, Polish Academy of Sciences, Rabiniańska 8, 87-100, Toruń, Poland

<sup>8</sup>Astronomisches Institut, Ruhr-Universität Bochum, Universitätsstrasse 150, D-44801 Bochum, Germany

<sup>9</sup>Instituto de Astronomía, Universidad Católica del Norte, Avenida Angamos 0610, Antofagasta, Chile

<sup>10</sup>Astroinformatik, Heidelberg Institute for Theoretical Studies, Schloss-Wolfsbrunnengasse 35, D-69118 Heidelberg, Germany

<sup>11</sup>University of Hawaii, Institute for Astronomy, 640 N. Aohoku Place, Hilo, HI 96720, USA

<sup>12</sup>Astronomical Institute, University of Wrocław, M. Kopernika 11, 51-622 Wrocław, Poland

Received 2021 September 30; revised 2021 December 21; accepted 2021 December 21; published 2022 March 8

## Abstract

We present time-series photometry of 21 nearby type II Cepheids in the near-infrared  $J$ ,  $H$ , and  $K_s$  passbands. We use this photometry, together with the Third Gaia Early Data Release parallaxes, to determine for the first time period–luminosity relations (PLRs) for type II Cepheids from field representatives of these old pulsating stars in the near-infrared regime. We found PLRs to be very narrow for BL Herculis stars, which makes them candidates for precision distance indicators. We then use archival photometry and the most accurate distance obtained from eclipsing binaries to recalibrate PLRs for type II Cepheids in the Large Magellanic Cloud (LMC). Slopes of our PLRs in the Milky Way and in the LMC differ by slightly more than  $2\sigma$  and are in a good agreement with previous studies of the LMC, Galactic bulge, and Galactic globular cluster type II Cepheids samples. We use PLRs of Milky Way type II Cepheids to measure the distance to the LMC, and we obtain a distance modulus of  $18.540 \pm 0.026$  (stat.)  $\pm 0.034$  (syst.) mag in the  $W_{JK}$  Wesenheit index. We also investigate the metallicity effect within our Milky Way sample, and we find a rather significant value of about  $-0.2$  mag dex<sup>-1</sup> in each band meaning that more metal-rich type II Cepheids are intrinsically brighter than their more metal-poor counterparts, in agreement with the value obtained from type II Cepheids in Galactic globular clusters. The main source of systematic error on our Milky Way PLRs calibration, and the LMC distance, is the current uncertainty of the Gaia parallax zero-point.

*Unified Astronomy Thesaurus concepts:* Type II Cepheid variable stars (2124); Pulsating variable stars (1307); Large Magellanic Cloud (903); Milky Way Galaxy (1054); Distance indicators (394); Galaxy distances (590); Stellar distance (1595); Population II Cepheid variable stars (1283); Population II stars (1284)

*Supporting material:* machine-readable tables

## 1. Introduction

The distinction between Classical Cepheids (CCeps) and type II Cepheids (T2Ceps; Baade 1944, 1958) led to the revision of the cosmic distance scale and significantly increased the measured distances to galaxies and, by extension, the timescale of the universe. Mixing these two classes of pulsating stars for the distance determination using the Leavitt Law (Period–Luminosity Relation, PLR; Leavitt 1908) as a standard candle results in a significant inaccuracy as T2Ceps are 1.5–2 mag fainter than CCeps of similar periods. CCeps remain the most important distance indicators, acting as an anchor for the local cosmic

distance scale and determination of the Hubble Constant (Riess et al. 2021). Less luminous T2Ceps are not as famous; however, they are crucial objects for tracing old stellar populations in our Galaxy, nearby galaxies, and globular clusters (Braga et al. 2018). Their lower brightness and abundance ( $\sim 10,000$  CCeps and only  $\sim 300$  T2Ceps are observed in the Magellanic Clouds; Soszyński et al. 2017a, 2018) make them more difficult to observe in other galaxies and to apply them as extragalactic distance indicators. However, there are objects like, e.g., globular clusters or dwarf spheroidal galaxies in which CCeps are not observed at all, and T2Ceps can be applied as distance tracers in these instances, more effectively than RR Lyrae stars as T2Ceps are 1–4 mag brighter.

T2Ceps are divided based on their period distributions (Gingold 1985) into three subgroups: BL Herculis (BL Her) type stars with periods between  $\sim 1$  and  $\sim 5$  days, W Virginis (W Vir) type stars with periods between  $\sim 5$  and  $\sim 20$  days, and

RV Tauri (RV Tau) stars with periods longer than  $\sim 20$  days. This distinction is not strict and depends on the environment. Stars belonging to each group present different light-curve morphologies and are most probably at different evolutionary stages. Soszyński et al. (2008) separated another subgroup of T2Ceps in the Magellanic Clouds that are usually called peculiar W Virginis (pW Vir, pWV) stars as they cover a similar range of periods as “classical” W Vir stars but are usually brighter, bluer and show different light-curve morphology from W Vir stars. Many of these peculiar stars were found to be in binary systems (Soszyński et al. 2017b).

Evolutionary channels leading to the formation of T2Ceps are not fully explained, but these sources are low metallicity ([Fe/H] between  $\sim -2.5$  and  $\sim 0$  dex) and most probably low-mass ( $0.5-1M_{\odot}$ ) stars crossing the Instability Strip during transition from the blue horizontal branch to the asymptotic giant branch in the case of BL Her stars, as a result of the helium-shell-flashes for W Vir stars and post asymptotic giant branch in the case of RV Tau stars (Bono et al. 1997; Wallerstein 2002). Detailed studies of two pW Vir stars in the Large Magellanic Cloud (LMC) resulted in the first dynamical mass determination for T2Ceps (Pilecki et al. 2017, 2018;  $0.64 \pm 0.02$  and  $1.51 \pm 0.09 M_{\odot}$ ). Pilecki et al. (2018) conclude that pW Vir stars are products of binary evolution (similar to Binary Evolution Pulsators; Pietrzyński et al. 2012), and they are much younger than other T2Ceps. Recent studies of the spatial distribution of T2Ceps in the Magellanic Clouds (Iwanek et al. 2018), as well as infrared excess in the Spectral Energy Distribution and the Light-time Travel Effect search in T2Ceps light curves (Groenewegen & Jurkovic 2017), suggest that the W Vir subgroup might be a mixture of old and intermediate stellar populations, and it is possible that these stars are the result of the binary evolution. Amplitude and period variations are common for T2Ceps (Rabidoux et al. 2010; Neilson et al. 2016), particularly among W Vir and RV Tau type stars, which can be partially explained by their evolution and movement across the Instability Strip (Neilson et al. 2016), but binarity, period modulations, period doubling, and chaotic dynamics also contribute (Moskalik & Buchler 1990; Smolec 2016; Plachy et al. 2017; Smolec et al. 2018). Almost all known T2Ceps pulsate in the fundamental mode (Bono et al. 1997). Two first-overtone stars were found among the LMC T2Ceps by Soszyński et al. (2019).

T2Ceps could be useful for determining distances of galaxies up to several megaparsecs using existing instruments (Majaess et al. 2009). PLRs of T2Ceps have been investigated empirically in the optical and near-infrared domain, by many authors, in the neighboring Large and Small Magellanic Clouds (Alcock et al. 1998; Matsunaga et al. 2011; Ciechanowska et al. 2010; Ripepi et al. 2015; Bhardwaj et al. 2017a; Soszyński et al. 2018), Galactic globular clusters (GGCs; Matsunaga et al. 2006), and Galactic bulge (GB; Soszyński et al. 2011; Braga et al. 2018), while theoretical work is so far very limited compared to CCeps or RR Lyrae stars (Di Criscienzo et al. 2007; Das et al. 2021). Ripepi et al. (2019) provided PLRs for T2Ceps in the solar neighborhood in the Gaia optical bands using parallaxes from the Gaia Data Release 2. According to these studies, period distributions vary between systems, and PLRs are linear for BL Her and W Vir stars, while steepening for RV Tau stars. Non-negligible metallicity effect on the absolute brightness of T2Ceps was found by Matsunaga et al. (2006) and by Das et al. (2021) but with opposite signs. Matsunaga et al. (2006) also suggested that RR Lyrae variables and T2Ceps create a common linear PLR in the near-infrared regime. The zero-point of the T2Cep distance scale was

calibrated by Feast et al. (2008) based on the Hipparcos parallaxes of two nearby stars, VY Pyx and  $\kappa$  Pav, and pulsational parallaxes of  $\kappa$  Pav, V553 Cen, and SW Tau.

As radially pulsing stars, T2Ceps also offer the possibility of measuring semi-geometrical distances with the Baade-Wessexlink technique (Feast et al. 2008), but studies of their projection factor (translating apparent radial velocity into the velocity of the pulsating surface of the star) are limited just to a few pioneering works (e.g., Balog et al. 1997; Breiterfeldt et al. 2015; Pilecki et al. 2017). A very good summary of our current knowledge about T2Ceps and efforts made to use them as distance indicators can be found in the recent review papers by Beaton et al. (2018) and Bhardwaj (2020).

Currently, the Gaia space mission (Gaia Collaboration et al. 2016) provides an unprecedented 6-dimensional map of our stellar neighborhood. This gives us an opportunity to use nearby stars of the general field with parallaxes known to within 1% accuracy to set the zero-point of the cosmic distance scale with similar accuracy. In this study, we present the first calibration of PLRs of T2Ceps in the Milky Way (MW) using near-infrared time-series photometry and the Third Gaia Early Data Release (EDR3; Gaia Collaboration 2020) parallaxes of nearby representatives of this class of pulsating stars. Presented work opens a series of publications of the Araucaria Project (Pietrzyński et al. 2002; Gieren et al. 2005) regarding the calibration of different distance indicators using multiband time-series photometry and spectroscopy of nearby stars and Gaia parallaxes. The Araucaria project was started in 2002, and our main motivation is precision calibration of the cosmic distance scale and determination of the local value of the Hubble Constant ( $H_0$ ) with 1% accuracy. Cosmic distances and, by extension,  $H_0$  uncertainty are dominated by systematic errors, and high accuracy can be achieved only by using several independent and precise types of distance indicators to determine the distance to a given object and compare the results.

The publication is organized as follows: in Section 2, we describe our observations, photometry, and determination of absolute mean magnitudes of our target stars in the MW as well as preparation of the LMC photometry. Section 3 presents calibration of PLRs, investigation of the effect of metallicity on T2Ceps magnitudes and measurement of the distance to the LMC. We discuss our results in Section 4 and summarize our work and prospects for the future in Section 5.

## 2. Data

### 2.1. The Milky Way

#### 2.1.1. Sample Selection

From the SIMBAD<sup>13</sup> and AAVSO<sup>14</sup> databases, we selected stars classified as T2Ceps with estimated distances from previous studies smaller than 5kpc from the Sun as the expected accuracy of Gaia parallaxes for stars at such distances is better than 5%. At such level of precision, bias on absolute magnitudes inferred from parallaxes should be negligible (see, e.g., Lutz & Kelker 1973; Feast & Catchpole 1997; Arenou & Luri 1999). Another selection criterion was the V-band magnitude. We discarded stars fainter than 13 mag in the V-band, as for such stars we would not be able to obtain precision (S/N  $\sim 100$ ) near-infrared photometry with a 0.8m telescope.

<sup>13</sup> <http://simbad.u-strasbg.fr/simbad/>

<sup>14</sup> <http://www.aavso.org/vsx/index.php?view=search.top>

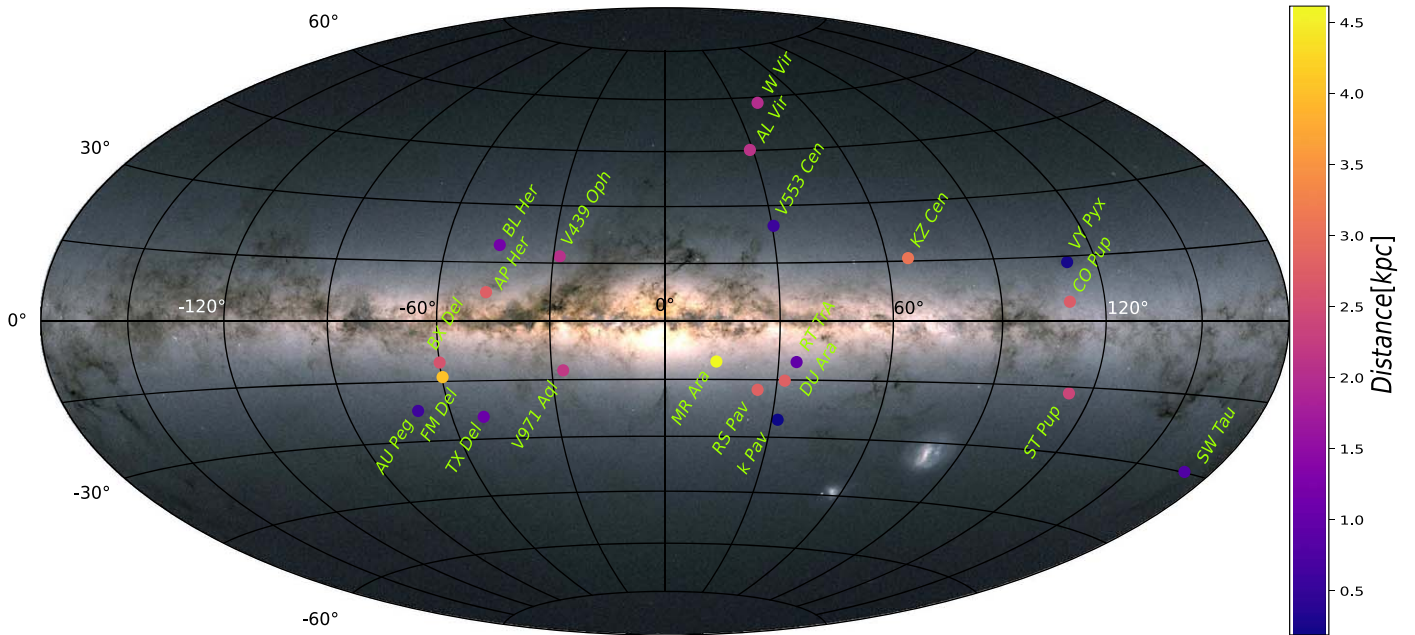


**Figure 1.** The Gaia photometric map of the Milky Way with marked positions of T2Ceps considered in this work. Color denotes the distance of a given star from the Sun.

We adopted a boundary period of 20 days to distinguish stars belonging to W Vir and RV Tau subclasses. The latter was not considered as these stars do not obey common linear PLR in both the Large and Small Magellanic Clouds. For 19 stars from this starting sample, we collected photometric data in  $J$ ,  $H$ , and  $K_s$  bands closely imitating the Two Micron All Sky Survey (2MASS) system (Skrutskie et al. 2006). Figure 1 presents positions of stars considered in this study plotted on the Gaia photometric map of the MW.

### 2.1.2. NIR Observations and Data Reductions

Observations were handled between 2017 February and 2020 March using the 0.81 m InfraRed Imaging Survey (IRIS) telescope equipped with  $1k \times 1k$  HAWAII detector (resulting in  $7' \times 7'$  field of view), located in Observatorio Cerro Armazones (OCA) in Chile (Hodapp et al. 2010; Ramolla et al. 2016). The saturation limit of IRIS is  $\sim 7.8$  mag in  $H$  and  $\sim 7.5$  mag in  $J$  and  $K_s$  passbands. For one star (VY Pyx), we used a neutral density (ND) filter blocking 97% of the light. This filter allowed us to observe stars up to  $\sim 4$  mag. The ND filter was not cooled; thus it produced thermal radiation reducing the precision of our photometry. Some of our targets were at a saturation limit, so we use exposures that were slightly defocused or taken during worse seeing conditions to ensure that they are not saturated. We aimed to cover the full light curve of every star, and in many cases, we collected 15–30 data points in each band. In some cases, we were only able to collect a few points so far, but our data are uniformly distributed over the pulsation cycle, which allows us to determine the mean magnitudes with satisfactory precision without using templates.

IRIS always takes short exposure (with the shortest possible exposure time of 2.2 s) and long exposure with specified exposure time (14.5 s) one by one. In order to estimate and subtract the sky background, each field was observed in 10 dithered positions. Raw exposures were sky-subtracted and flat-fielded using standard IRAF (Tody 1986) routines. An

astrometric solution was performed with Sextractor (Bertin & Arnouts 1996) and SCAMP (Bertin 2006), and then 10 dithered frames were resampled and combined with SWARP (Bertin 2010) into a single, final image (details of the pipeline used for calibrations can be found in Watermann 2012). Aperture photometry was performed with the DAOPHOT (Stetson 1987) package, and instrumental photometry was tied to the 2MASS system using the constant stars present in a given field as standards (usually more than 3 stars of brightness similar to our target with quality flag AAA in the 2MASS catalog). If there were no comparison stars of similar magnitude in a given field (cases of VY Pyx, SW Tau, and AL Vir), we used long exposures (14.5 s) to measure the brightness of comparison stars while the target was measured in the short exposure (2.2 s). We found a non-negligible color term in  $J$  band, and it amounts to  $-0.07$  ( $J - K_s$ ). Internal precision of our photometry is at a level of 0.02 mag. In order to check correctness of our transformation to the 2MASS system, we compared the magnitudes of the constant stars present in the observed fields (transformed to the 2MASS system using an approach identical to our scientific objects) with the corresponding magnitudes from the 2MASS catalog. The observed fields offered very limited numbers of bright constant stars; thus for this test, we mostly used sources that were adopted as comparison stars in the transformation of the photometry of science targets. Each considered star was excluded from the set of comparison stars while transforming its own photometry. This test is presented in Figure 2. The mean difference between IRIS and 2MASS photometry is zero with the error on the mean of 0.002 mag in each band. We adopt this value as our zero-point uncertainty, which contributes to the systematic error of our calibration of PLRs.

For 3 bright T2Ceps— $\kappa$  Pav, V553 Cen, and SW Tau—archival infrared photometry collected at the South African Astronomical Observatory with the MkII photometer installed on the 0.75 m telescope is available (Feast et al. 2008). We

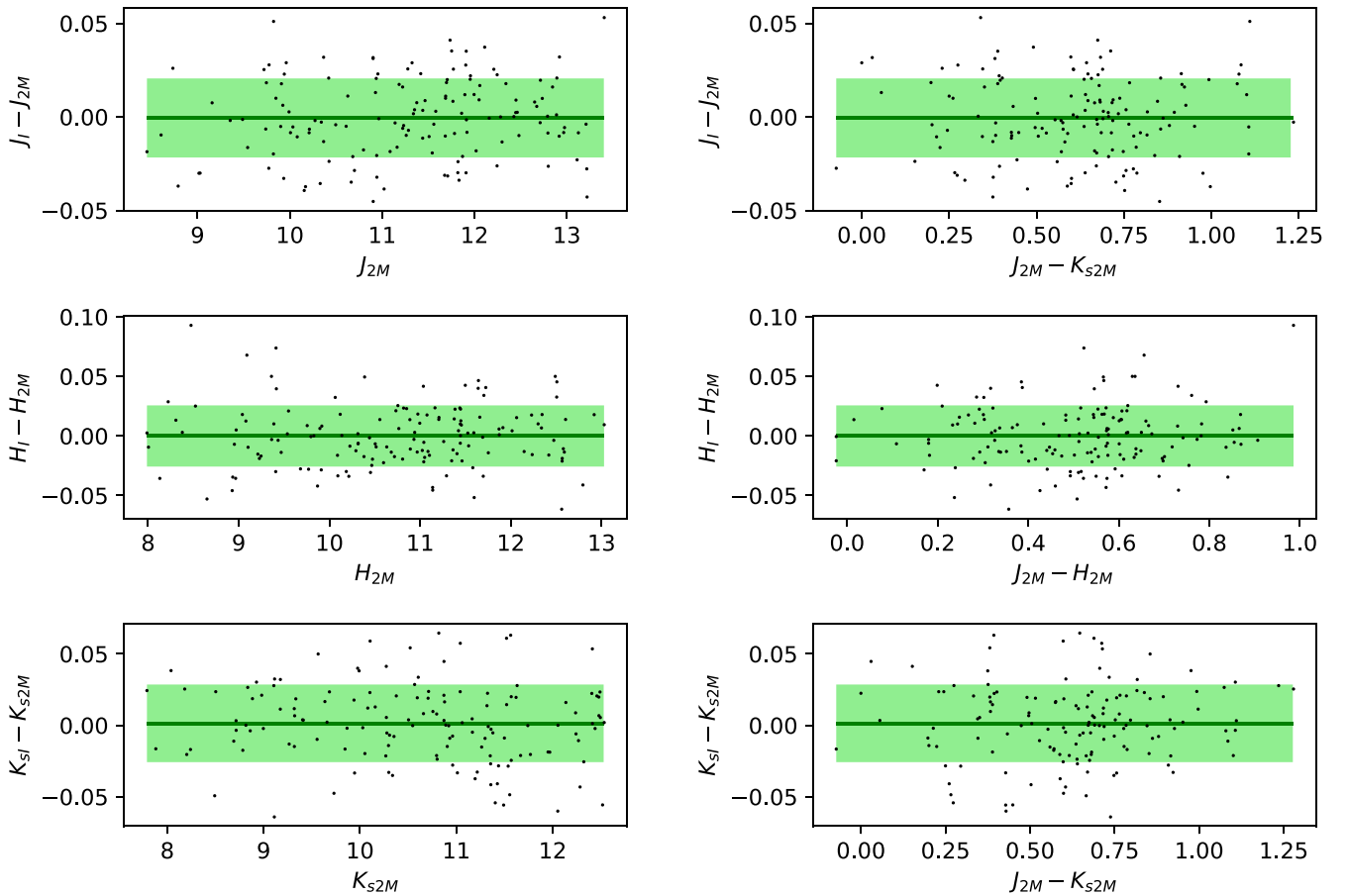


**Figure 2.** Test of the accuracy of our transformations of IRIS photometry from instrumental to the 2MASS system. Magnitudes of constant stars observed by IRIS and transformed to the 2MASS system are compared with corresponding values from the 2MASS catalog. Typical error in the y-axis is 0.03 mag (errorbars are not plotted for clarity). Green lines mark the mean difference between our measurement and 2MASS catalog, and it is consistent with zero in all bands with the error on the mean 0.002 mag. Light-green area denotes rms, which amounts to 0.022 mag in  $J$  and 0.025 mag in  $H$  and  $K_s$  passbands.

transform these photometric data to the 2MASS system using formulae from Koen et al. (2007).

Small fraction of time-series photometry used in this work is presented in Table 1. Its full version is provided as supplementary material online.

### 2.1.3. Optical Photometry and Periods

We searched for well-sampled optical photometry for determining periods of T2Ceps. For most of our stars, ASAS-SN (Kochanek et al. 2017) and ASAS (Pojmanski 2002) photometry in  $V$  band is available; although in some cases, light curves were very noisy. Some T2Ceps had been observed by Berdnikov (2008), and we also collected our own optical photometric data in  $V$  band with the 0.4 m VYSOS 16 telescope located in OCA. VYSOS 16 data were processed using the same procedure as in the case of IRIS, and aperture photometry was performed with DAOPHOT. Then we roughly standardized the light curves using a single comparison star and its ASAS-SN magnitude. If the quality of ASAS-SN or ASAS light curve was satisfactory, we preferred these sources as they contain hundreds of observations; while in the case of observations from Berdnikov and VYSOS16, only a few dozen data points were collected. We adopted photometry for 8 stars (BL Her, RT TrA, V553 Cen, AU Peg, AL Vir, CO Pup, W Vir, and MR Ara) from ASAS, 9 stars from ASAS-SN (BX Del, KZ Cen, V971 Aql, DU Ara, V439 Oph, FM

Del, AP Her, ST Pup, and RS Pav), 1 star from Berdnikov ( $\kappa$  Pav), and 3 stars from our own VYSOS 16 data (VY Pyx, SW Tau, and TX Del).

Primarily, we adopted the periods available in the AAVSO database, and with these initial values, we tried to find the value that yielded the smoothest light curve using `fnpeaks` code.<sup>15</sup> Figures 3 and 4 present our collection of  $V$ -band light curves for our sample phased with the final periods and zero-phase set to the intensity-averaged mean value on the rising branch. Periods are given in column 2 of Table 2.

### 2.1.4. Mean Magnitudes and Extinction

In order to determine mean magnitudes of our infrared light curves, we transformed magnitudes into fluxes and modeled each light curve using the following Monte Carlo procedure. For each data point of a given light curve, we generated a random synthetic data point from the Gaussian distribution centered on the original data point value with the standard deviation equal to the corresponding photometric uncertainty. Then an Akima spline, implemented in the `Python SciPy` module (Virtanen et al. 2020), was fitted to the synthetic light curve. Mean flux was calculated and transformed back into magnitude. We repeated this procedure 10,000 times. Fitting a

<sup>15</sup> <http://helas.astro.uni.wroc.pl/deliverables.php?active=fnpeaks>

**Table 1**  
Near-infrared Photometry of Milky Way T2Ceps.

| Star   | Filter   | HJD             | $m$<br>(mag) | $\sigma_m$<br>(mag) | Source |
|--------|----------|-----------------|--------------|---------------------|--------|
| AL Vir | <i>J</i> | 2,458,180.84288 | 8.486        | 0.012               | IRIS   |
| AL Vir | <i>J</i> | 2,458,181.85912 | 8.477        | 0.012               | IRIS   |
| AL Vir | <i>J</i> | 2,458,182.83384 | 8.379        | 0.018               | IRIS   |
| AL Vir | <i>J</i> | 2,458,199.75768 | 8.370        | 0.030               | IRIS   |
| AL Vir | <i>J</i> | 2,458,201.81562 | 8.486        | 0.016               | IRIS   |
| AL Vir | <i>J</i> | 2,458,202.79249 | 8.458        | 0.019               | IRIS   |
| AL Vir | <i>J</i> | 2,458,203.82118 | 8.324        | 0.011               | IRIS   |
| AL Vir | <i>J</i> | 2,458,204.76877 | 8.176        | 0.013               | IRIS   |
| AL Vir | <i>J</i> | 2,458,511.86068 | 8.359        | 0.015               | IRIS   |
| AL Vir | <i>J</i> | 2,458,555.87695 | 8.115        | 0.010               | IRIS   |
| AL Vir | <i>J</i> | 2,458,558.80783 | 8.208        | 0.030               | IRIS   |
| AL Vir | <i>J</i> | 2,458,559.82360 | 8.300        | 0.017               | IRIS   |
| AL Vir | <i>J</i> | 2,458,560.86504 | 8.353        | 0.030               | IRIS   |
| AL Vir | <i>J</i> | 2,458,561.84425 | 8.462        | 0.030               | IRIS   |
| AL Vir | <i>J</i> | 2,458,564.85894 | 8.174        | 0.015               | IRIS   |
| AL Vir | <i>J</i> | 2,458,567.77684 | 8.128        | 0.030               | IRIS   |
| AL Vir | <i>J</i> | 2,458,568.76634 | 8.215        | 0.013               | IRIS   |
| AL Vir | <i>J</i> | 2,458,569.83901 | 8.288        | 0.030               | IRIS   |
| AL Vir | <i>J</i> | 2,458,571.84169 | 8.428        | 0.030               | IRIS   |
| AL Vir | <i>J</i> | 2,458,580.80998 | 8.342        | 0.030               | IRIS   |
| AL Vir | <i>J</i> | 2,458,581.81409 | 8.435        | 0.014               | IRIS   |
| AL Vir | <i>J</i> | 2,458,582.82497 | 8.469        | 0.014               | IRIS   |
| AL Vir | <i>J</i> | 2,458,583.81693 | 8.470        | 0.030               | IRIS   |
| AL Vir | <i>J</i> | 2,458,585.79749 | 8.146        | 0.014               | IRIS   |
| AL Vir | <i>J</i> | 2,458,586.81269 | 8.089        | 0.030               | IRIS   |
| AL Vir | <i>J</i> | 2,458,587.75078 | 8.115        | 0.030               | IRIS   |
| AL Vir | <i>J</i> | 2,458,588.78209 | 8.144        | 0.011               | IRIS   |
| AL Vir | <i>J</i> | 2,458,599.78980 | 8.170        | 0.012               | IRIS   |
| AL Vir | <i>H</i> | 2,458,180.84864 | 8.084        | 0.013               | IRIS   |
| AL Vir | <i>H</i> | 2,458,182.82839 | 8.228        | 0.030               | IRIS   |
| AL Vir | <i>H</i> | 2,458,201.82129 | 8.101        | 0.030               | IRIS   |
| AL Vir | <i>H</i> | 2,458,202.79827 | 8.132        | 0.010               | IRIS   |
| AL Vir | <i>H</i> | 2,458,203.82692 | 8.191        | 0.016               | IRIS   |
| AL Vir | <i>H</i> | 2,458,204.77439 | 8.054        | 0.015               | IRIS   |
| AL Vir | <i>H</i> | 2,458,511.86675 | 8.203        | 0.016               | IRIS   |
| AL Vir | <i>H</i> | 2,458,555.88273 | 7.860        | 0.030               | IRIS   |
| AL Vir | <i>H</i> | 2,458,558.80238 | 7.879        | 0.015               | IRIS   |

Gaussian to the resulting histogram of mean magnitudes gives us the final mean magnitude and its uncertainty. Our results are given in columns 10–15 of Table 2, and phased light curves are presented in Figures 5–10. SW Tau is the only star that has observations both from IRIS and MkII photometer, and obtained light curves are in a very good agreement.

Apparent mean magnitudes have to be corrected for interstellar extinction. We used Schlafly & Finkbeiner (2011) reddening maps to obtain the color excess  $E(B - V)$  in the direction of each star. For the nearest stars in our sample, such reddening can be overestimated, so we implement the following procedure from Drimmel & Spergel (2001). We assume an axisymmetric distribution of the dust density in the Galaxy:

$$\rho(r, z) = \rho_0 \exp(-r/r_D - |z|/z_D) \quad (1)$$

where  $r$  is the radial coordinate with respect to the galactic center, and  $z$  is the distance from the galactic plane; we estimated the contribution of dust located between us and the target star to the total  $E(B - V)$  value in a given direction.

Detailed description of the model used in this process can be found in Suchomska et al. (2015). Final values of  $E(B - V)$  for our sample stars are given in column 17 of Table 2, and in most cases, they do not differ significantly from the original values from the Schlafly & Finkbeiner (2011) map. Adopting the reddening law from Cardelli et al. (1989) and O’Donnell (1994) and  $R_V = 3.1$ , we calculated total-to-selective extinction  $R_\lambda = A_\lambda/E(B - V)$  for each band. Our results are 0.892, 0.553, and 0.363 for  $J$ ,  $H$ , and  $K_s$  respectively. As our systematic uncertainty of extinction corrections, we adopt 0.02 mag in  $J$  and  $H$  and 0.01 mag in  $K_s$  passband, and these values should contain both the uncertainty of the determined  $E(B - V)$  values and the adopted reddening law for calculating  $R_\lambda$ .

Moreover, we calculated the quasi-magnitude Wesenheit index  $W_{JK_s} = K_s - R_{JK_s} \times (J - K_s)$ , which, if the correct reddening law is used, should be independent of the reddening (Madore 1982). We calculated  $R_{JK_s} = A_{K_s}/(A_J - A_{K_s})$  again using Cardelli et al. (1989) with the assumption of  $R_V = 3.1$ , which gives us  $W_{JK_s} = K_s - 0.69 \times (J - K_s)$ . The Wesenheit index should be in principle reddening free; however, there might be some systematic error related to the adopted reddening law. We assume this error to be at the level of 0.01 mag.

### 2.1.5. Distances

The distances to our T2Ceps come from Gaia EDR3 parallaxes (Lindgren et al. 2021b; column 3 of our Table 2) corrected for the zero-point offset (ZPO) as determined with the dedicated Python code<sup>16</sup> described in Lindgren et al. (2021a; column 5 of our Table 2). We increase the parallax uncertainties by 10% as suggested by Riess et al. (2021) to account for possible excess uncertainty, and resulting uncertainties are given in column 4 of Table 2. According to Lindgren et al. (2021a), the uncertainty of the zero-point is 5  $\mu\text{as}$ , which is equivalent to 0.024 mag in absolute magnitudes calculated using Gaia EDR3 parallaxes for the median parallax of our sample (0.45 mas), so we adopt 0.024 mag as a systematic uncertainty related to parallaxes zero-point on our absolute magnitudes and, by extension, on the PLRs determination. We adopt the Renormalised Unit Weight Error (RUWE) and the Goodness-of-Fit (GOF) parameters as parallax quality indicators. These parameters were found to be relevant for CCeps by Breuval et al. (2021) and Riess et al. (2021). RUWE should be close to 1, and not higher than 1.4 (Lindgren et al. 2021b), while good values of GOF according to Riess et al. (2021) are below 12.5. Higher values of these parameters indicate, e.g., saturation of the star in Gaia photometry or its photocenter movement due to binarity. RUWE and GOF values for our T2Ceps are given in columns 6 and 7 of Table 2. Stars with RUWE > 1.4 and GOF > 12.5, namely TX Del,  $\kappa$  Pav, and ST Pup, are not used for PLRs calibration. Inverting parallaxes yields distances  $d$  in kiloparsecs, and from such distances, we calculated distance moduli  $\mu = 5 \log d - 2$  (column 8 of Table 2). Distance moduli are subtracted from the mean magnitudes (corrected for extinction) to obtain the absolute magnitudes. We do not use these values directly to fit PLRs, but we use the Astrometric Based Luminosity (ABL) instead, which is explained in Section 3.1. Colors of markers in Figure 1 denote the distances of the studied T2Ceps.

<sup>16</sup> [https://gitlab.com/icc-ub/public/gaiadr3\\_zero\\_point](https://gitlab.com/icc-ub/public/gaiadr3_zero_point)

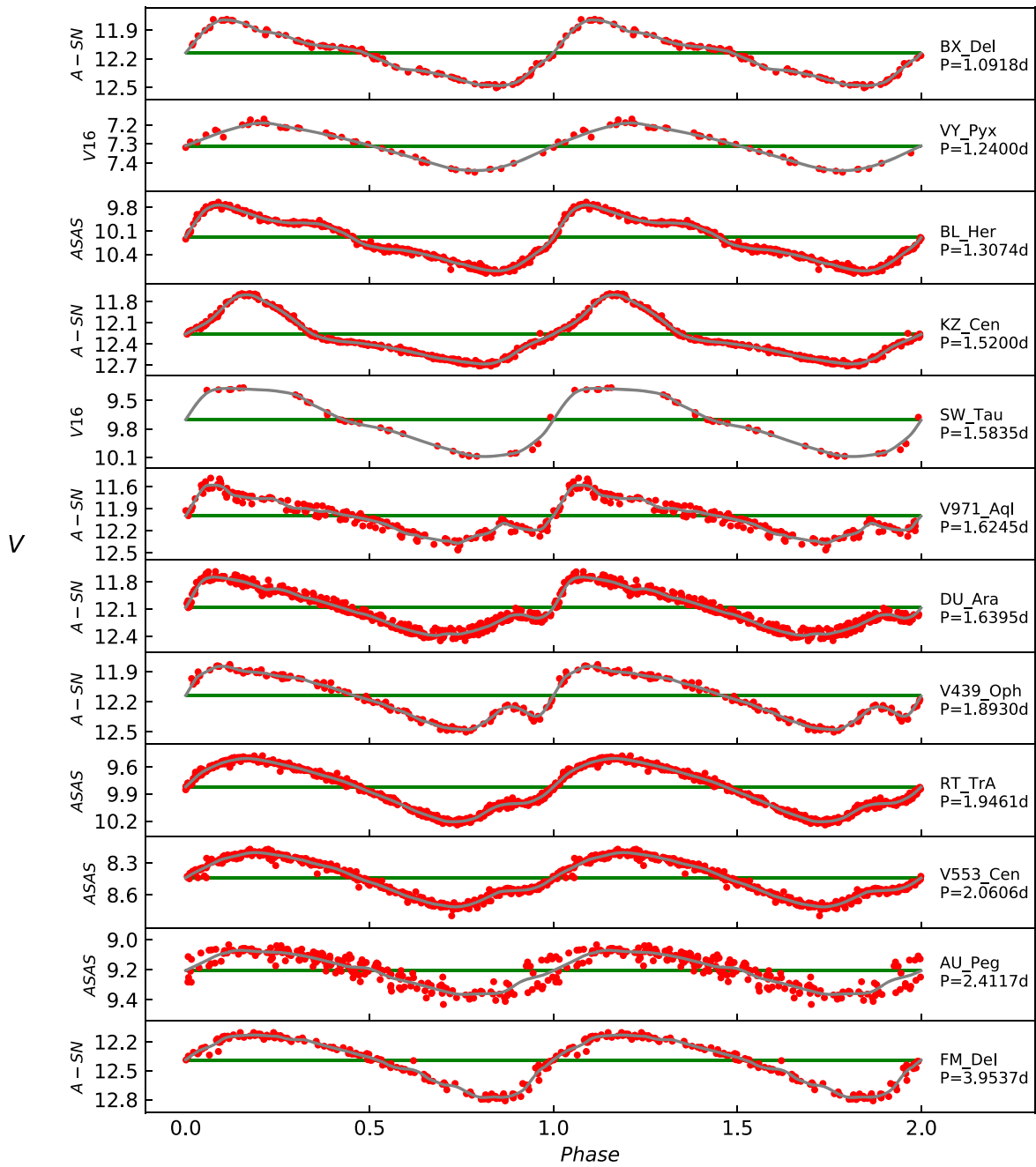


**Figure 3.** V-band light curves of BL Her stars. Meaning of labels is as follows: A-SN corresponds to ASAS-SN data, V16 denotes VYSOS 16, and B08 is Berdnikov (2008). Green line is the mean magnitude.

## 2.2. The Large Magellanic Cloud

### 2.2.1. Sample Selection, Periods, and Photometry

The most complete list of T2Ceps in the LMC is the OGLE catalog (Soszyński et al. 2018), so we adopt classification and periods from this source (we exclude RV Tau and pW Vir stars from this initial sample). Infrared photometry from several sources is available, e.g., Vista Magellanic Clouds Survey (VMC; Ripepi et al. 2015), Large Magellanic Cloud Synoptic Survey (LMCSS; Bhardwaj et al. 2017a), and the InfraRed Survey Facility (IRSF; Matsunaga et al. 2011). We preferentially use mean magnitudes determined from time-series photometry over the single-point measurement, so we use VMC for  $J$  and  $K_s$  passbands ( $H$  band is not provided). We adopt mean magnitudes of T2Ceps from

Table 4 in Ripepi et al. (2015). For  $H$  band, we initially used LMCSS data but obtained a LMC distance modulus that was significantly smaller ( $\sim 0.2$  mag) than in  $J$  and  $K_s$  passbands, while IRSF phase-corrected  $H$ -band magnitudes give a value consistent with  $J$  and  $K_s$ . In Figure 11, we plot the difference between  $H$ -band LMCSS mean magnitudes (data from Table 4 in Bhardwaj et al. 2017a), and IRSF (data from Table 1 in Matsunaga et al. 2011) phase-corrected magnitudes for T2Ceps present in both sources, and the mean difference between the two samples is close to  $-0.2$  mag. We do not know the origin of this discrepancy, and we present results using both LMCSS and IRSF photometry, but the IRSF sample is used for further analysis. Uncertainties of IRSF magnitudes given in Matsunaga et al. (2011), in their Table 1, do not take into account statistical uncertainties related to the

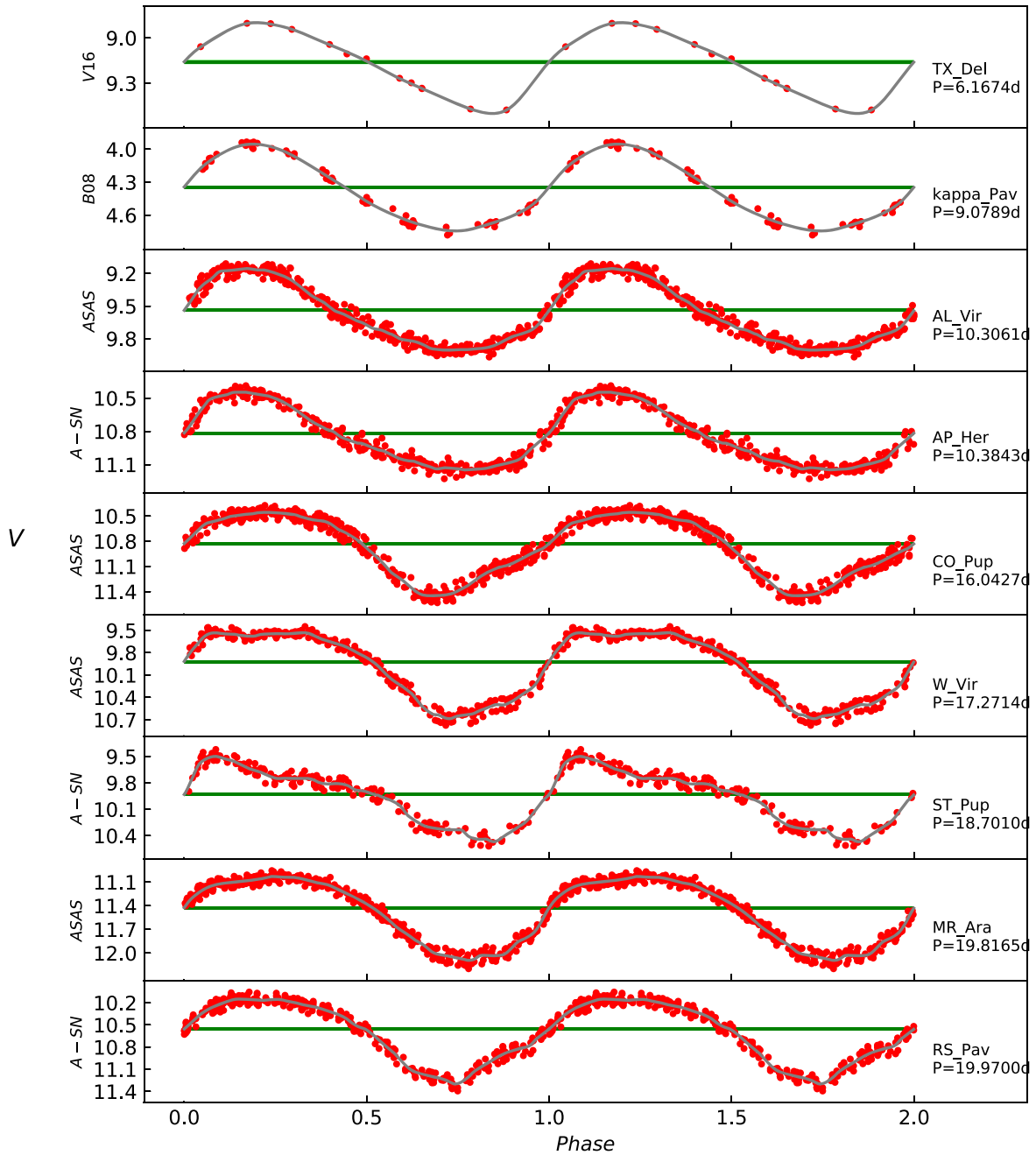


**Figure 4.** V-band light curves of W Vir stars. Meaning of labels is the same as in Figure 3.

phase-correction. We assume that they are at the level of 0.05 mag, and we add this value quadratically to the given  $H$ -band uncertainty.

Photometry of MW T2Ceps is in the 2MASS system; thus we have to transform LMC data into 2MASS as well. LMCSS photometry is already provided in the 2MASS system. IRSF was transformed using formulae given in Kato et al. (2007). VMC photometry is in the VISTA system, so we transformed it to the 2MASS using the respective formulae from CASU.<sup>17</sup> We adopt 0.02 mag as a systematic uncertainty for the VMC (photometric zero-point accuracy) mean magnitudes. Ripepi et al. (2015) found a difference of about 0.05 mag between T2Ceps PLRs zero-points in  $J$  and  $K_s$  based on the VMC mean magnitudes

and the IRSF phase-corrected data. The difference is caused mainly by the systematic error associated with applying phase-correction for the IRSF single-point observation based on  $I$ -band light-curve amplitude. We then adopt 0.05 mag as a systematic uncertainty for the IRSF  $H$ -band mean magnitudes.

Figure 12 presents a map of the LMC, with marked positions of our final sample of T2Ceps, and Table 3 contains a compilation of the data used in the analysis.

### 2.2.2. Extinction and Distances

We estimate the extinction toward LMC T2Ceps using the recent maps of Górski et al. (2020) based on red clump stars. From the map, we obtain  $E(B - V)$  color excess for each star (column 11 of Table 3). We use again Cardelli et al. (1989) and O'Donnell (1994) and  $R_V = 3.1$  to calculate total extinction in each

<sup>17</sup> <http://casu.ast.cam.ac.uk/surveys-projects/vista/>



**Table 2**  
Data of Milky Way T2Ceps

| Name         | $P$      | $\pi$  | $\sigma_\pi$ | ZPO     | RUWE | GOF   | $\mu$  | $\sigma_\mu$ | $\langle J \rangle$ | $\sigma_J$ | $\langle H \rangle$ | $\sigma_H$ | $\langle K_s \rangle$ | $\sigma_{K_s}$ | $E(B - V)$ | [Fe/H] |
|--------------|----------|--------|--------------|---------|------|-------|--------|--------------|---------------------|------------|---------------------|------------|-----------------------|----------------|------------|--------|
| (1)          | (2)      | (3)    | (4)          | (5)     | (6)  | (7)   | (8)    | (9)          | (10)                | (11)       | (12)                | (13)       | (14)                  | (15)           | (16)       | (17)   |
| BX Del       | 1.09180  | 0.3650 | 0.0150       | -0.0188 | 1.13 | 3.20  | 12.079 | 0.085        | 11.156              | 0.024      | 10.930              | 0.033      | 10.873                | 0.024          | 0.100      | -0.2   |
| VY Pyx       | 1.23995  | 3.9495 | 0.0186       | -0.0237 | 0.89 | -3.57 | 7.004  | 0.010        | 6.029               | 0.013      | 5.761               | 0.017      | 5.696                 | 0.039          | 0.048      | -0.4   |
| BL Her       | 1.30744  | 0.8469 | 0.0179       | 0.0016  | 1.29 | 10.20 | 10.365 | 0.046        | 9.206               | 0.014      | 9.017               | 0.015      | 8.932                 | 0.013          | 0.067      | -0.1   |
| KZ Cen       | 1.52004  | 0.3024 | 0.0153       | -0.0224 | 1.20 | 5.51  | 12.442 | 0.103        | 11.302              | 0.033      | 11.051              | 0.027      | 10.987                | 0.030          | 0.084      | ...    |
| SW Tau       | 1.58355  | 1.2244 | 0.0222       | -0.0103 | 1.25 | 5.52  | 9.542  | 0.039        | 8.320               | 0.007      | 8.082               | 0.007      | 7.955                 | 0.008          | 0.252      | 0.2    |
| V971 Aql     | 1.62453  | 0.4400 | 0.0219       | -0.0175 | 1.26 | 5.10  | 11.698 | 0.105        | 10.508              | 0.014      | 10.199              | 0.016      | 10.112                | 0.017          | 0.174      | ...    |
| DU Ara       | 1.63949  | 0.3394 | 0.0180       | -0.0189 | 1.25 | 7.52  | 12.228 | 0.110        | 10.923              | 0.017      | 10.665              | 0.015      | 10.580                | 0.024          | 0.055      | ...    |
| V439 Oph     | 1.89298  | 0.4753 | 0.0163       | -0.0103 | 1.17 | 4.68  | 11.569 | 0.073        | 10.367              | 0.014      | 9.969               | 0.016      | 9.855                 | 0.020          | 0.268      | ...    |
| RT TrA       | 1.94612  | 1.0162 | 0.0162       | -0.0021 | 0.95 | -1.85 | 9.961  | 0.035        | 8.553               | 0.014      | 8.331               | 0.019      | 8.200                 | 0.015          | 0.112      | ...    |
| V553 Cen     | 2.06055  | 1.7286 | 0.0224       | -0.0080 | 0.94 | -0.97 | 8.801  | 0.028        | 7.242               | 0.016      | 6.976               | 0.017      | 6.869                 | 0.017          | 0.069      | ...    |
| AU Peg       | 2.41174  | 1.6463 | 0.0200       | -0.0180 | 1.25 | 6.79  | 8.894  | 0.026        | 7.787               | 0.014      | ...                 | ...        | 7.066                 | 0.015          | 0.046      | -0.2   |
| FM Del       | 3.95373  | 0.2300 | 0.0135       | -0.0174 | 0.93 | -1.71 | 13.033 | 0.119        | 11.08               | 0.017      | 10.729              | 0.024      | 10.646                | 0.017          | 0.087      | ...    |
| TX Del       | 6.16742  | 0.9078 | 0.0294       | -0.0112 | 1.94 | 27.9  | 10.183 | 0.070        | 7.836               | 0.011      | ...                 | ...        | 7.460                 | 0.011          | 0.085      | 0.5    |
| $\kappa$ Pav | 9.07890  | 5.2451 | 0.1221       | 0.0046  | 2.29 | 37.6  | 6.403  | 0.051        | 3.201               | 0.021      | 2.881               | 0.021      | 2.784                 | 0.021          | 0.019      | ...    |
| AL Vir       | 10.30611 | 0.4574 | 0.0190       | -0.0152 | 0.98 | -0.32 | 11.627 | 0.088        | 8.270               | 0.011      | 7.956               | 0.013      | 7.887                 | 0.013          | 0.072      | -0.4   |
| AP Her       | 10.38432 | 0.3578 | 0.0152       | -0.0028 | 1.13 | 3.74  | 12.215 | 0.092        | 9.034               | 0.032      | 8.630               | 0.030      | 8.520                 | 0.030          | 0.373      | -0.7   |
| CO Pup       | 16.04266 | 0.3471 | 0.0166       | -0.0212 | 1.31 | 9.29  | 12.169 | 0.115        | 8.975               | 0.017      | 8.534               | 0.013      | 8.415                 | 0.019          | 0.155      | -0.6   |
| W Vir        | 17.27137 | 0.4728 | 0.0222       | -0.0227 | 1.06 | 2.13  | 11.525 | 0.098        | 8.442               | 0.012      | 8.117               | 0.014      | 8.029                 | 0.016          | 0.036      | -1.0   |
| ST Pup       | 18.7010  | 0.4099 | 0.0232       | -0.0091 | 2.07 | 25.6  | 11.889 | 0.121        | 8.472               | 0.008      | 8.118               | 0.007      | 7.944                 | 0.011          | 0.120      | ...    |
| MR Ara       | 19.81649 | 0.2087 | 0.0236       | -0.0080 | 0.97 | -0.75 | 13.321 | 0.237        | 9.817               | 0.032      | 9.421               | 0.059      | 9.279                 | 0.041          | 0.110      | ...    |
| RS Pav       | 19.96997 | 0.3547 | 0.0157       | -0.0003 | 0.99 | -0.26 | 12.249 | 0.097        | 8.799               | 0.018      | 8.353               | 0.02       | 8.231                 | 0.018          | 0.072      | ...    |

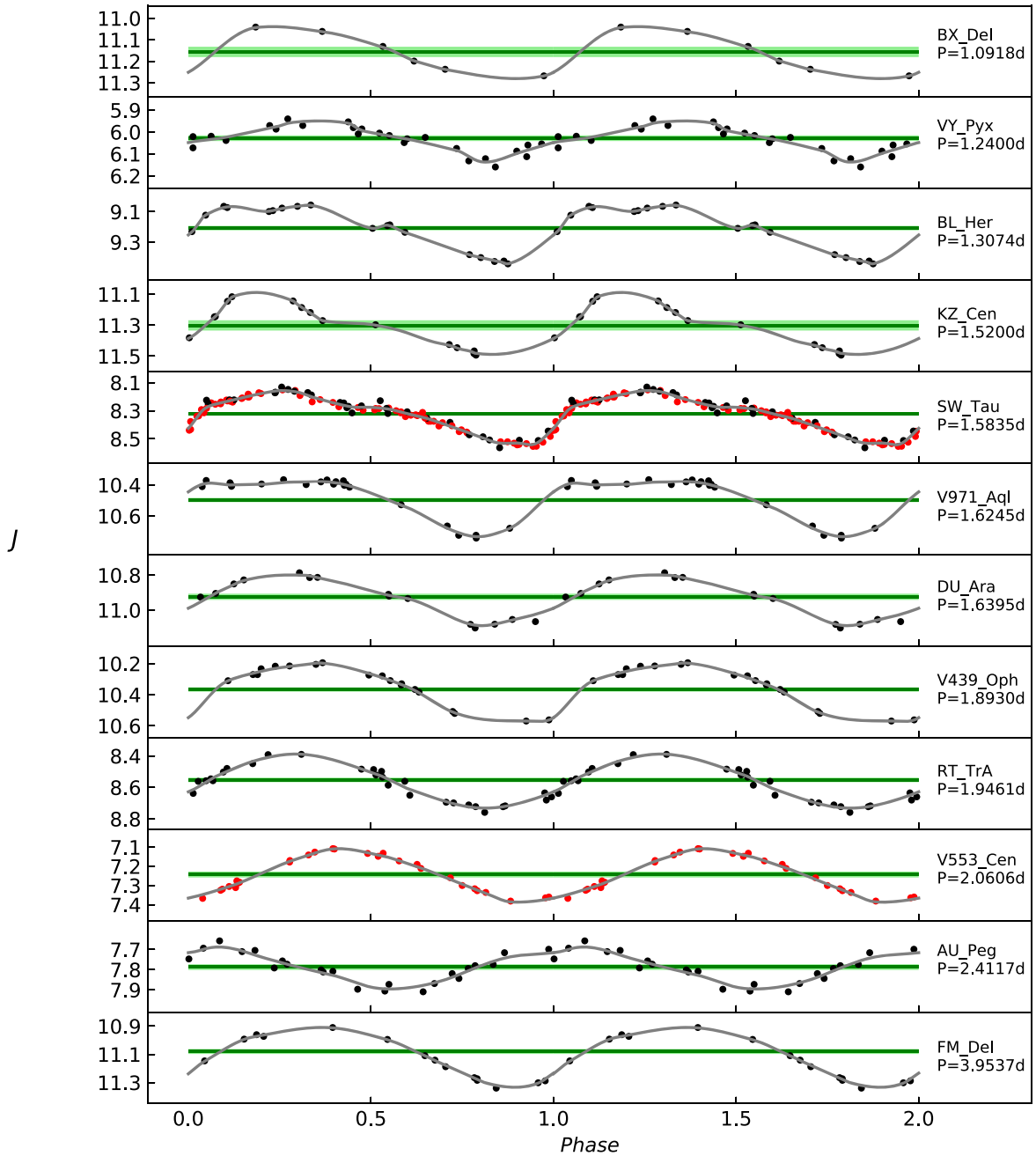


**Figure 5.** *J*-band light curves of BL Her stars. Black points are measurements from IRIS, red are from Feast et al. (2008). Green line is the mean magnitude while light green denotes its  $1\sigma$  uncertainty.

photometric band. Statistical errors of  $E(B - V)$  given in the map are below 0.01 mag, but we adopt 0.01 mag for each star. Systematic error of the reddening is related mostly to the uncertainty of the intrinsic color of the red clump. Górski et al. (2020) estimated the uncertainty of the intrinsic red clump color in the LMC to be 0.013 mag for the  $(B - V)$  color index; thus we adopt 0.01 mag for the systematic uncertainty related to the reddening in each band.

The most accurate distance to the LMC was obtained using late-type eclipsing binaries by Pietrzyński et al. (2019). They obtained the distance modulus of  $18.477 \pm 0.004(\text{stat.}) \pm 0.026(\text{syst.})$  mag, and such value is subtracted from reddening-corrected mean magnitudes in order to calculate absolute magnitudes. We also calculated individual corrections related to the geometry of the LMC. We adopt the plane-disk model of the LMC from van

der Marel & Cioni (2001). We assume the same definition of the LMC center as in Pietrzyński et al. (2019) ( $\alpha_0 = 5^{\text{h}}20^{\text{m}}$ ,  $\delta_0 = -69^{\circ}18'$ ), the LMC inclination  $i = 25^{\circ}$ , and the line-of-nodes position angle  $\theta = 132^{\circ}$  (also from Pietrzyński et al. 2019). Calculated corrections are presented in column 12 of Table 3, and they are subtracted from absolute magnitudes. Distribution of RR Lyrae stars in the LMC (Jacyszyn-Dobrzeńicka et al. 2017; Cusano et al. 2021) shows that the old population stars form a spherical halo around the LMC disk; thus the line-of-sight depth effect should have a significant impact on the spread of LMC T2Ceps PLRs; however, it is not possible to apply any corrections for this effect. We suspect that the depth effect is at the level of 0.1 mag, so we add quadratically such value to the uncertainty of each star.

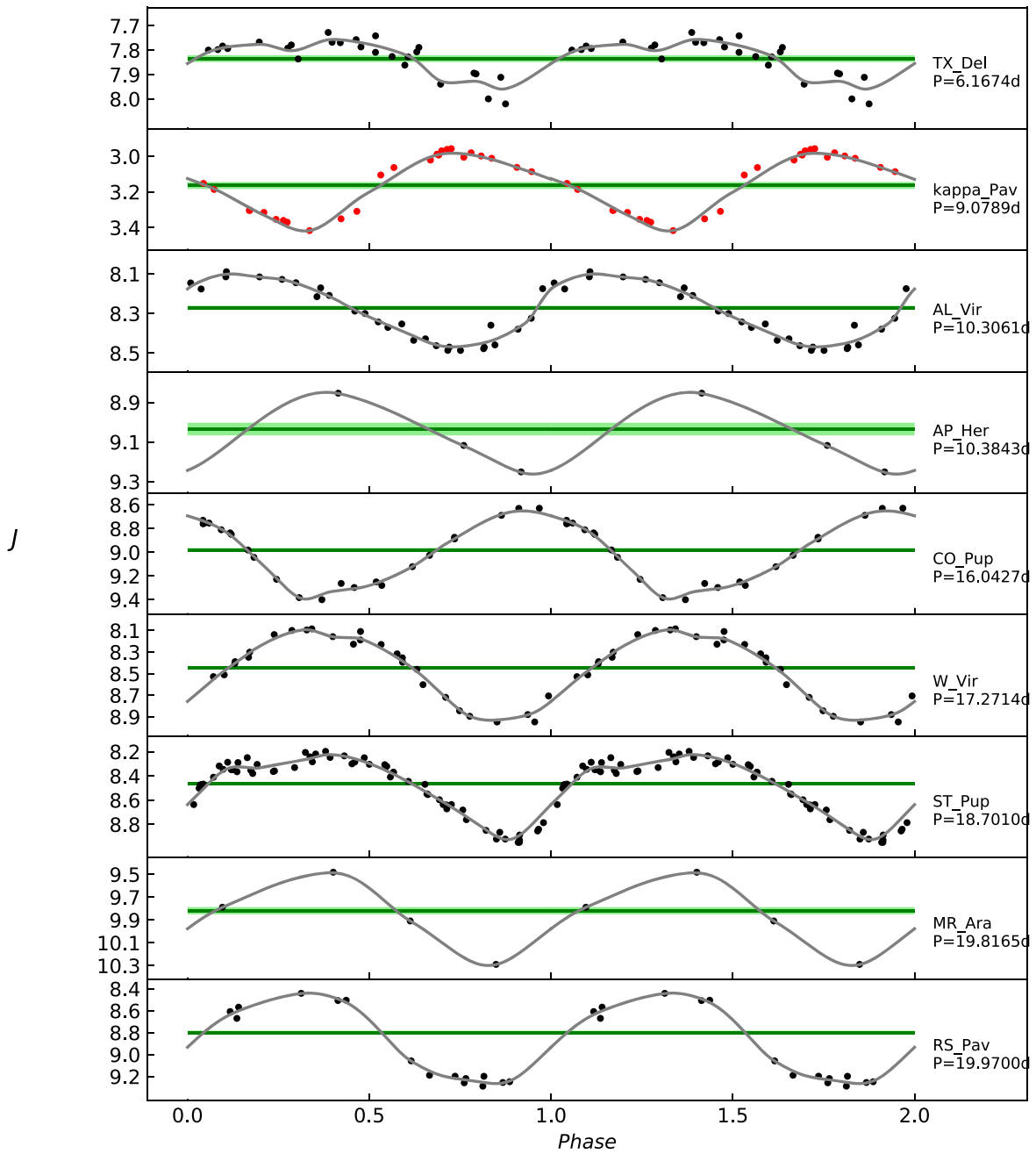


Figure 6.  $J$ -band light curves of W Vir stars. Meaning of colors and lines is the same as in Figure 5.

### 3. Analysis and Results

#### 3.1. MW

Before determining PLRs, we have to take a closer look at our MW sample to check if it contains pW Vir stars. As we mentioned in the introduction, pW Vir stars are usually more luminous and bluer than regular W Vir stars of similar periods, and have different light-curve morphologies. Visually comparing the shapes of optical light curves of W Vir stars with LMC T2Ceps optical light curves from the OGLE Atlas of Variable Star Light Curves<sup>18</sup> (Soszyński et al. 2018), we suspect that three stars,  $\kappa$  Pav, AP Her, and AL Vir, are pW Vir stars.  $\kappa$  Pav has already been suggested to be a member of pW Vir subgroup by Feast et al.

(2008). Breitfelder et al. (2015) studied this star in detail using photometric, interferometric, and spectroscopic data and did not find signatures of a companion star, while it is believed that pW Vir stars are binaries (Soszyński et al. 2017b). On the other hand, the  $RUWE$  and  $GOF$  parallax quality parameters of  $\kappa$  Pav are higher than the recommended values, which can be the result of its binarity. Figures 13 and 14 present  $K_s$  band absolute magnitude and  $J - K_s$  color index as a function of period for our MW sample (red, green, and blue denotes BL Her, W Vir, and pW Vir stars respectively) and LMC BL Her (pink), W Vir (light green), and pW Vir (cyan) stars from the VMC survey (Ripepi et al. 2015). Absolute magnitudes of the LMC sample were calculated by correcting VMC mean magnitudes for extinction using Górski et al. (2020) reddening maps, the Cardelli et al. (1989) reddening law, and the LMC distance modulus of 18.477 mag from Pietrzyński et al. (2019).

<sup>18</sup> <http://ogle.astrouw.edu.pl/atlas/>

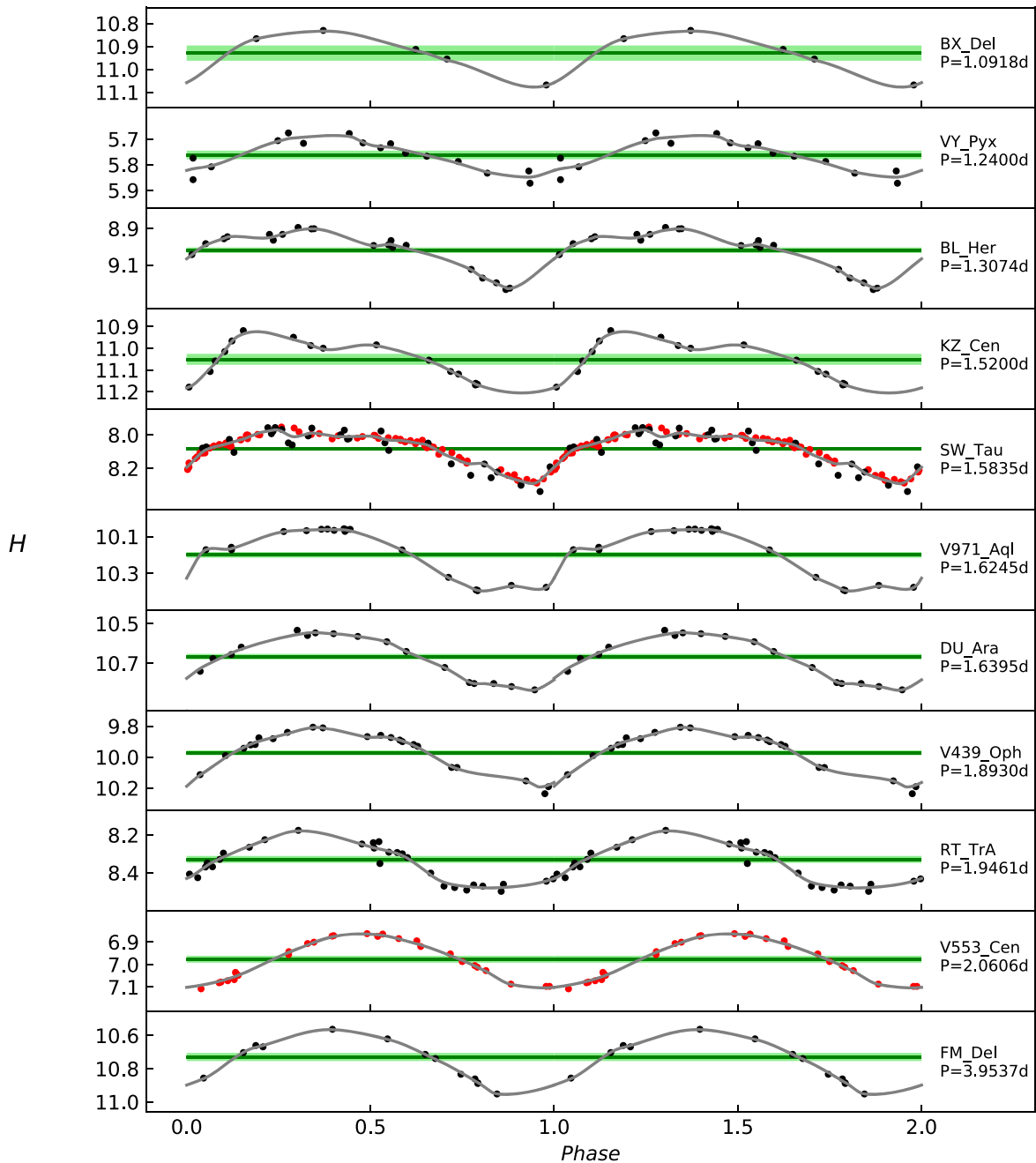
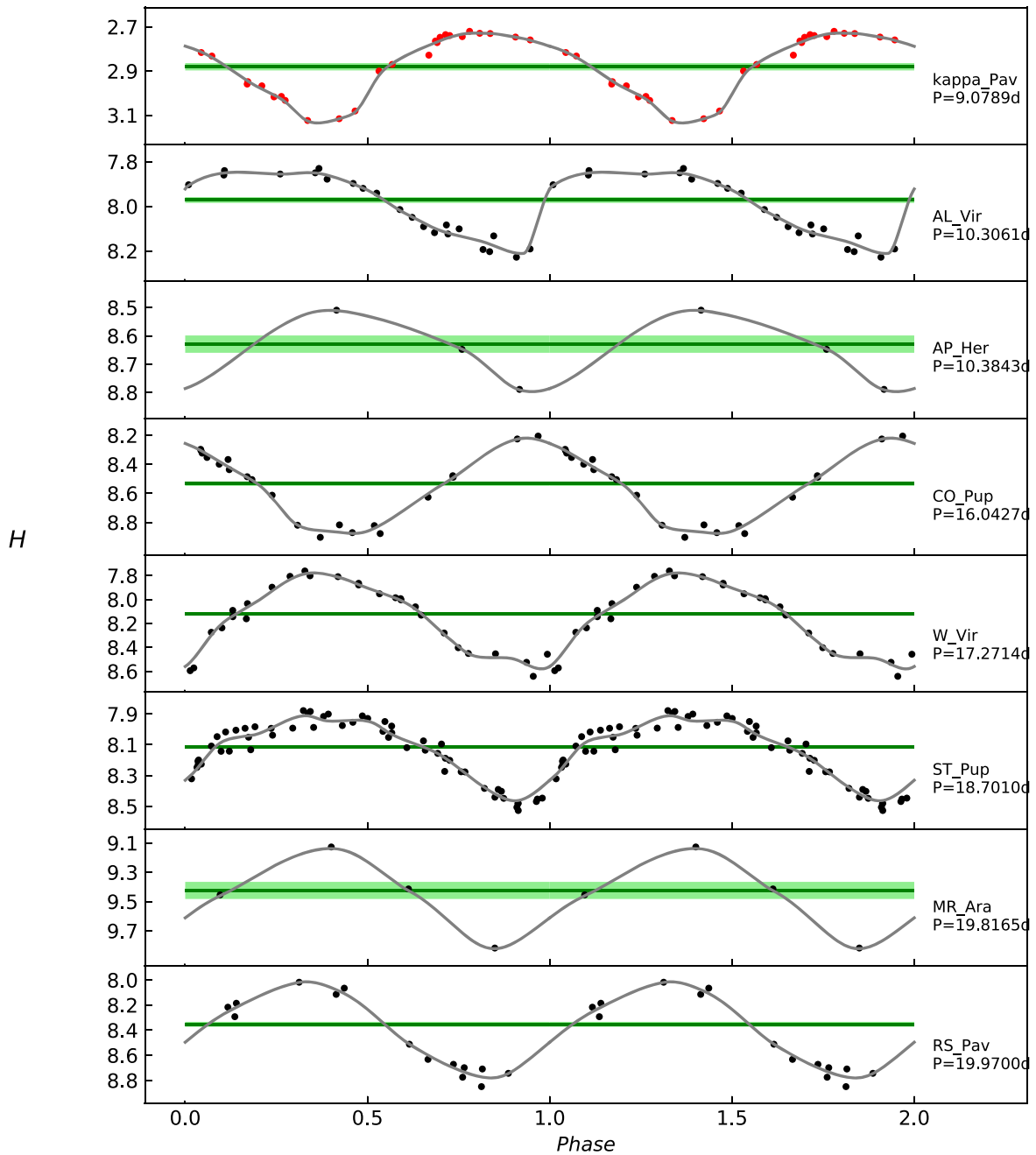


Figure 7.  $H$ -band light curves of BL Her stars. Meaning of colors and lines is the same as in Figure 5.

The three stars mentioned above are overlapping with a *clump* of pW Vir stars in the LMC in Figure 13. AL Vir and AP Her are also bluer than the other W Vir stars in our sample, lying in a range of colors of the LMC pW Vir stars, while  $\kappa$  Pav is rather located among W Vir, although some LMC pW Vir stars are also placed among W Vir stars on this diagram. This, in our opinion, confirms that AP Her and AL Vir are pW Vir type stars, and  $\kappa$  Pav is most probably peculiar as well, so we do not consider these stars in further analysis.

Another interesting object from the point of view of colors is AU Peg; it is very red ( $J - K_s \approx 0.7$  mag) compared to other BL Her type stars ( $J - K_s \approx 0.3$  mag). Harris et al. (1984) found this star to be a member of a single-lined spectroscopic binary with a more massive compact object as a companion and a dusty envelope surrounding the system. Its optical light curve

(Figure 3) presents significant instabilities in pulsations, and Jurkovic et al. (2007) suggested that this star is a double mode CCep, but its position on our period–luminosity diagram shows clearly that it is a T2Cep. Further analysis shows that the deviation of AU Peg from the PLR decreases for longer wavelengths and vanishes in the Wesenheit index. It suggest that this deviation is caused by high extinction, much higher than estimated in Schlafly & Finkbeiner (2011). We decided to exclude this star from fitting PLRs in  $J$ ,  $H$ , and  $K_s$  passbands. According to Harris et al. (1984), the contribution of the non-pulsating component of this system to the total brightness is very low, so we include AU Peg in our PLRs fit for the Wesenheit index (excluding AU Peg in the Wesenheit index does not affect our results).



**Figure 8.** *H*-band light curves of W Vir stars. Meaning of colors and lines is the same as in Figure 5.

Another star that was found to be in a binary system is TX Del (Harris & Welch 1989). This star is not included in the PLR calibration as its RUWE and GOF parameters are higher than acceptable values, but it is interesting to discuss its observed properties. Its position on the period–luminosity diagram does not deviate from the relation determined by the LMC sample, but it is on the blue side of the color index range of LMC W Vir stars; thus it is another pW Vir candidate.

W Vir star—a subgroup prototype—is yet another star drawing attention. It is significantly fainter (0.2–0.5 mag) than the other W Vir type stars on the period–luminosity diagram. Its deviation from the PLR is higher for longer wavelengths and in the Wesenheit index. On the other hand, its position on the period–color diagram does not deviate significantly from the other W Vir stars, but it is located among the bluest LMC W

Vir stars. Kovtyukh et al. (2011) analyzed emission lines in the W Vir spectrum and concluded that this star is surrounded by an envelope. Such an envelope could be a possible explanation for the faintness; however, the wavelength dependence of the effect is opposite to what is expected from extinction. This star is also exceptional as it shows the period doubling effect in its light curves (Templeton & Henden 2007), which makes it similar to RV Tau stars. We decided to determine PLRs including and excluding this star (cases 1 and 2, respectively). We also calibrate PLRs for BL Her stars solely (case 3).

Absolute mean magnitudes of MW T2Ceps derived in Section 2.1 are plotted against the logarithm of periods in Figure 15. We want to find the slope  $a$  and intercept  $b$  of the PLR:

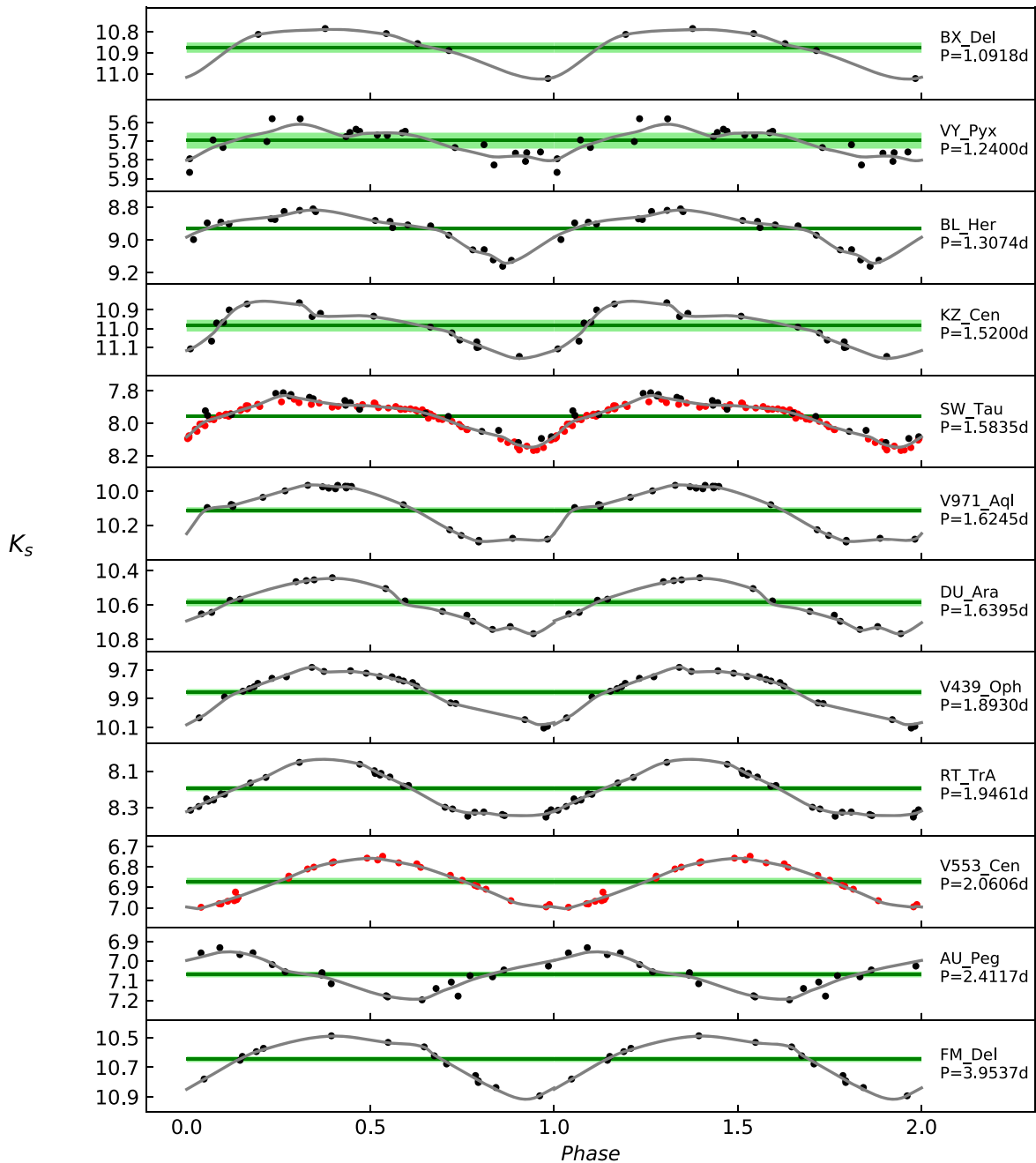


**Figure 9.**  $K_s$ -band light curves of BL Her stars. Meaning of colors and lines is the same as in Figure 5.

$$M_\lambda = a_\lambda(\log P - \log P_0) + b_\lambda \quad (2)$$

where  $P_0$  is the median period of the sample, and for MW T2Ceps,  $\log P_0 = 0.3$ . In order to avoid biases related to inversion of parallaxes, it is suggested to use the ABL (Feast & Catchpole 1997; Arenou & Luri 1999). ABL is defined as follows:

$$\text{ABL} = \pi 10^{0.2m_\lambda - 2} = 10^{M_\lambda/5} \quad (3)$$

where  $\pi$  is the parallax in milliarcseconds, and  $m_\lambda$  and  $M_\lambda$  are the apparent (corrected for extinction) and absolute magnitudes in the given band  $\lambda$ , respectively. We calculate ABL for the stars in our sample, and parameters  $a$  and  $b$  with their uncertainties are determined using Monte Carlo simulations

and the curvefit routine from the Python SciPy module. We run 10,000 simulations in each passband, and in each simulation we generate a random sample of magnitudes and parallaxes from the normal distributions defined by the mean magnitudes and parallaxes and uncertainties of these values. Slopes and intercepts with corresponding errors are listed in Table 4.

### 3.2. LMC

Figure 16 presents the period–luminosity diagrams for LMC T2Ceps. Using the least squares method and  $3\sigma$  clipping (twice), we fit the lines in the form of Equation (2) (with  $\log P_0 = 0.7$  for the whole sample and  $\log P_0 = 0.3$  when using BL Her stars solely) to obtain the slopes and intercepts of these

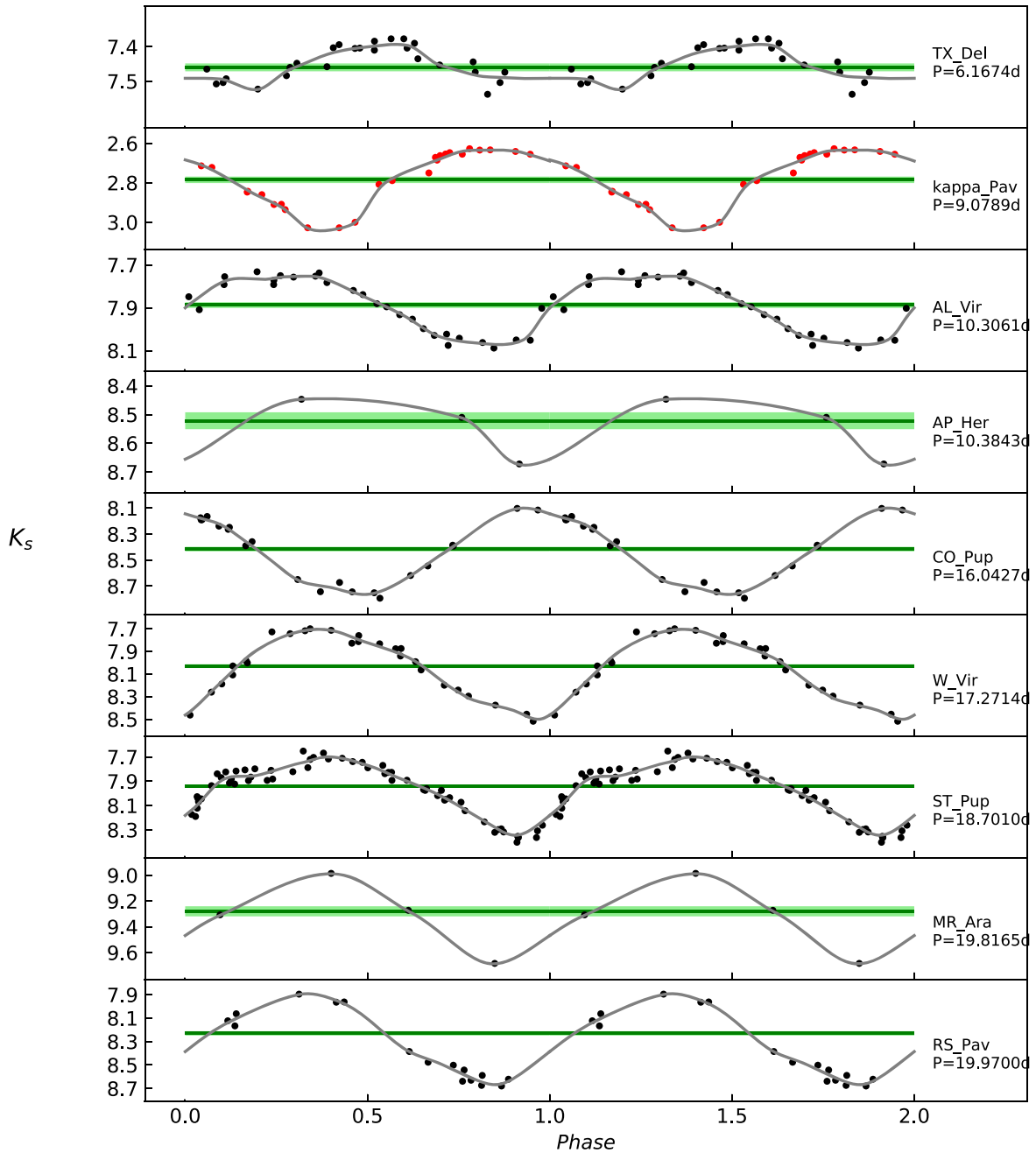


**Figure 10.**  $K_s$ -band light curves of W Vir stars. Meaning of colors and lines is the same as in Figure 5.

relations. Resulting PLRs for LMC T2Ceps are presented in Table 5 (zero-points of PLRs for BL Her+W Vir are recalculated for  $\log P_0 = 0.3$ ) and plotted in Figure 16 with green lines. Dispersion of the PLR and also the number of  $3\sigma$  outliers is much higher in  $H$  band than in other bands, which is expected because for  $H$  band, we used mean magnitudes inferred from a single measurement. In Figure 16, we also plot PLRs of MW T2Ceps obtained in the previous section, and we notice that PLRs are steeper in the LMC in each passband, with a difference greater than  $2\sigma$ . The observed spread of LMC PLRs is significantly greater than for MW T2Ceps, which clearly shows that distances of MW T2Ceps are determined with a very high precision.

Forcing the MW slopes for PLRs of T2Ceps in the LMC, we can measure the distance to the LMC. We use mean apparent

magnitudes of LMC T2Ceps corrected for extinction and for the LMC geometry. We fit the lines in the form of Equation (2) (using  $\log P_0$  as above) with the slope fixed on the corresponding value from MW relations using the least squares method with  $3\sigma$  clipping applied twice. We repeat this fitting using BL Her stars solely and forcing the slope to the corresponding value from MW BL Her stars. Coefficients of fitted lines are listed in Table 6. In column 7 of this table, we give the obtained distance modulus  $\mu$  of the LMC in each band. The result obtained from *LMCSS* photometry is more than 0.2 mag smaller than in other bands, which was already mentioned in Section 2.2. The obtained values in different bands generally agree within  $1\sigma$ , but we note that they are smaller in  $J$  band than in  $K_s$  band, and are highest in  $W_{JKS}$  Wesenheit index, which may be the result of some remaining

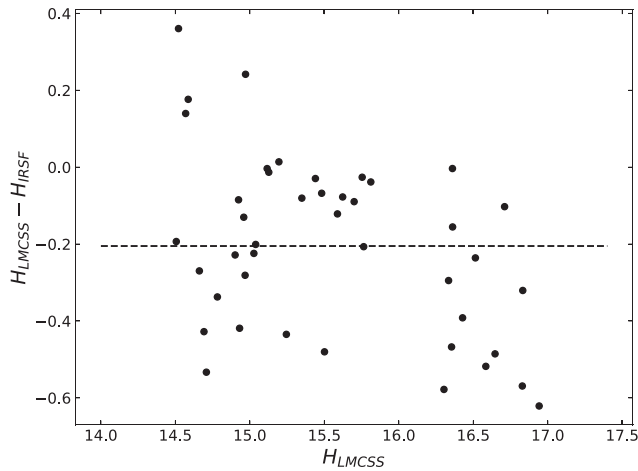


**Figure 11.** Comparison of LMC T2Ceps  $H$ -band mean magnitudes from LMCSS and IRSF catalogs. Dashed line represents the mean difference between these two sources of about  $-0.2$  mag.

color excess (underestimated or overestimated extinction toward MW and/or LMC T2Ceps). Results obtained with W Vir and BL Her stars are also in a good agreement ( $1\sigma$ – $2\sigma$ ) with the most precise value from eclipsing binaries (18.477), while using BL Her stars solely gives slightly higher distances.

### 3.3. The Metallicity Effect

The last column of Table 2 contains spectroscopic metallicity determinations  $[\text{Fe}/\text{H}]$  from Maas et al. (2007) for a fraction of T2Ceps from our MW sample. Uncertainties of these values are not given, so we assume  $\sigma_{\text{Fe}/\text{H}} = 0.1$  dex, which is a rather typical value for measurements of this parameter. Using these measurements and the determined PLRs, we investigate a possible metallicity effect on the absolute brightness of T2Ceps.

In Figure 17, we plot deviations of stars with known  $[\text{Fe}/\text{H}]$  from the PLRs determined in the previous section (in case 1) as a function of  $[\text{Fe}/\text{H}]$ . We continue to reject pW Vir stars and those with low-quality parallaxes (TX Del) and also AU Peg. Only 10 stars have metallicities available, and 3 of them are rejected, so our determination is hampered by poor statistics; however, a pretty clear trend is visible in each band. Using the least squares method (uncertainties are taken into account), we fit lines to these relations in 10,000 Monte Carlo simulations, and the slopes of these fits yield an estimation of the  $\gamma$  parameter, i.e., the influence of the metallicity on the T2Ceps absolute brightness. We fit lines in two cases: a common line for W Vir and BL Her stars (red line) and for BL Her stars solely (black line). Results of this fitting ( $\gamma$  values) are presented in Table 7, and they show a significant metallicity effect of the order of  $-0.2$  mag dex $^{-1}$  in each band and considered case, meaning that more metal-rich T2Ceps are intrinsically brighter than their more metal-poor counterparts. This result is in agreement with the value of  $-0.1$  mag dex $^{-1}$  obtained by Matsunaga et al. (2006) for T2Ceps in globular clusters. Recent empirical calibrations of the  $\gamma$  parameter for Classical Cepheids give a very similar value of the effect (Gieren et al. 2018; Breuval et al. 2021; Ripepi et al. 2021), while for RR Lyrae stars the sign of the relation is opposite (Nemec et al. 1994; Neeley et al. 2019).

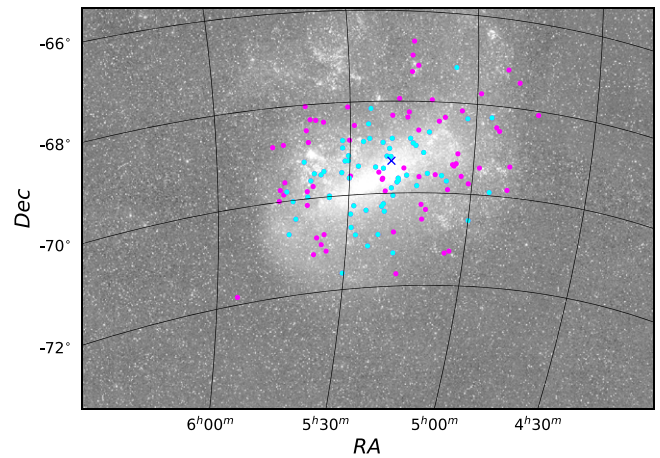


**Figure 12.** Positions of T2Ceps in the Large Magellanic Cloud considered in this study. Cyan points mark stars observed by the IRSF solely, while magenta points are stars present both in IRSF and VMC catalogs.

It is not possible at this point to apply any correction for the metallicity effect to the LMC distance as there are no metallicity determinations for the LMC T2Ceps in the literature, and the mean metallicity of our MW sample is not known; thus this effect still contributes to the error of our measurements.

## 4. Discussion

### 4.1. PLRs

Regarding the PLRs of the MW T2Ceps, we notice a very small dispersion for short period BL Her stars, which confirms that they are precise distance indicators. Another observation is that, on average, BL Her stars in the MW are brighter than in the LMC while for W Vir stars, the situation is the opposite (see Figure 16), and the difference between slopes of PLRs is at the level of  $2\sigma$ – $3\sigma$ . In light of found metallicity effect (assuming that this effect is identical for BL Her and W Vir stars), this could suggest that BL Her and W Vir stars have different mean metallicities. This would in turn support the conclusion of Iwanek et al. (2018), deduced from the spatial distribution of these two groups in the LMC, that BL Her and W Vir stars are not the same population of stars. In Table 8, we listed values of slopes of PLRs for T2Ceps in the LMC, GGCs, and the GB found in the literature. A general trend of increasing slope toward longer wavelengths is observed in each sample, which is in agreement with theoretical studies (e.g., Das et al. 2021). PLRs of T2Ceps in the LMC derived in this work are in a very good agreement with other studies of PLRs in this galaxy. MW PLRs are flatter than in other T2Ceps samples, and in most cases, they differ from other listed slopes by more than  $2\sigma$ . A very good agreement is observed between our MW PLRs and LMC PLRs from Bhardwaj et al. (2017a). Bhardwaj et al. (2017a) used mixed LMCSS and VMC photometry, but as we show in our analysis, LMCSS photometry might be problematic.

Having two independent zero-points of PLRs, one can average them; but as the slopes of MW and LMC PLRs are quite different, the influence of the metallicity on the absolute magnitudes might be strong, and the metallicity determinations of T2Ceps are very poor; we doubt that averaging would increase the precision of distances measured with such averaged PLRs. For the time being, we suggest using a single



**Table 3**  
Data of T2Ceps in the LMC.

| OGLE id <sup>1</sup> | $P$       | $\langle J \rangle$ | $\sigma_J$ | $\langle H_{\text{LMC}} \rangle$ | $\sigma_{H_{\text{LMC}}}$ | $\langle H_{\text{IRSF}} \rangle$ | $\sigma_{H_{\text{IRSF}}}$ | $\langle K_s \rangle$ | $\sigma_{K_s}$ | $E(B-V)$ | $\Delta m_{\text{geom}}$ |
|----------------------|-----------|---------------------|------------|----------------------------------|---------------------------|-----------------------------------|----------------------------|-----------------------|----------------|----------|--------------------------|
| (1)                  | (2)       | (3)                 | (4)        | (5)                              | (6)                       | (7)                               | (8)                        | (9)                   | (10)           | (11)     | (12)                     |
| 053                  | 1.0429993 | ...                 | ...        | ...                              | ...                       | 17.299                            | 0.05                       | ...                   | ...            | 0.131    | 0.003                    |
| 188                  | 1.0493152 | ...                 | ...        | ...                              | ...                       | 17.576                            | 0.09                       | ...                   | ...            | 0.179    | -0.025                   |
| 006                  | 1.0879277 | ...                 | ...        | ...                              | ...                       | 17.450                            | 0.07                       | ...                   | ...            | 0.105    | 0.034                    |
| 020                  | 1.1081258 | ...                 | ...        | ...                              | ...                       | 17.111                            | 0.06                       | ...                   | ...            | 0.104    | 0.020                    |
| 071                  | 1.1521741 | 17.536              | 0.022      | 16.832                           | 0.151                     | 17.297                            | 0.05                       | 17.324                | 0.026          | 0.117    | 0.004                    |
| 089                  | 1.1673093 | 17.732              | 0.018      | 16.829                           | 0.050                     | 17.209                            | 0.09                       | 17.476                | 0.043          | 0.104    | 0.006                    |

**Note.**<sup>1</sup> Full OGLE id contains prefix OGLE-LMC-T2CEP.

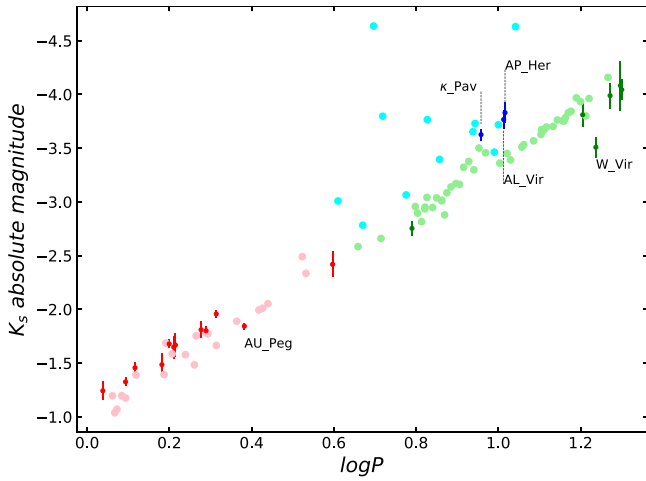


**Figure 13.**  $K_s$  band absolute magnitudes as a function of periods of pulsation for Milky Way and Large Magellanic Cloud T2Ceps. Red, green, and blue data points with errorbars are Galactic BL Her, W Vir, and peculiar W Vir stars respectively. Pink points are BL Her stars, light green denotes W Vir stars, and cyan denotes peculiar W Vir stars in the LMC (source Ripepi et al. 2015) shifted to obtain absolute magnitudes using LMC distance modulus from Pietrzyński et al. (2019).

anchor for the T2Ceps distance scale. Future determinations of metallicities of T2Ceps in both samples could allow for studies of a common period–luminosity–metallicity relationship.

An important issue to be discussed is the influence of the Gaia parallaxes ZPO on our MW PLRs. We calculated ZPO using Lindegren et al. (2021a), later called L21, from the  $G$  magnitude, color index, and ecliptic latitude of a given star, although recently Groenewegen (2021; G21) published their new estimation of the ZPO. Both L21 and G21 used quasars and detached binaries in their calibrations but different selection criteria for these objects. Following the procedure given in G21, we calculated ZPO for our stars. Table 9 contains Gaia IDs of our stars, HEALPix level giving the best quality of the ZPO (this parameter defines the resolution of the used ZPO map; for details, see Groenewegen 2021), and the obtained ZPO with errors, which are usually greater than values obtained using L21. We use these corrections to determine PLRs again (excluding W Vir, which is outlying also with G21 corrections). We also fit PLRs without introducing any ZPO corrections. The results are shown in Table 10. Not introducing ZPO does not affect slopes, while using G21 corrections gives shallower slopes of the PLRs, and the difference is slightly more than  $1\sigma$ . Zero-points of PLRs differ by  $\sim 0.04$  mag when

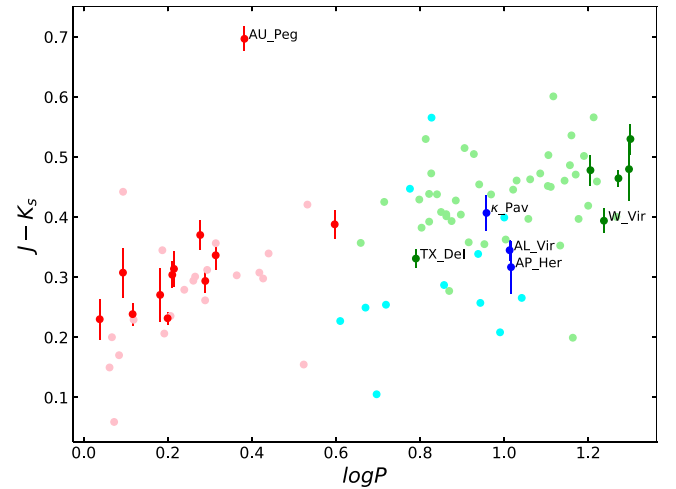


**Figure 14.** Color index of the Milky Way and LMC T2Ceps as a function of pulsational period. Markers colors are the same as in Figure 13.

**Table 4**  
Period–Luminosity Relations for Milky Way T2Ceps

| Filter     | $a$    | $\sigma_a$ | $b$    | $\sigma_b$ | $\sigma$ | Comment |
|------------|--------|------------|--------|------------|----------|---------|
| $J$        | -1.946 | 0.071      | -1.519 | 0.022      | 0.090    | case 1  |
|            | -2.005 | 0.084      | -1.525 | 0.023      | 0.062    | case 2  |
|            | -1.955 | 0.208      | -1.520 | 0.030      | 0.063    | case 3  |
| $H$        | -2.098 | 0.074      | -1.757 | 0.022      | 0.094    | case 1  |
|            | -2.173 | 0.088      | -1.766 | 0.023      | 0.041    | case 2  |
|            | -2.162 | 0.210      | -1.764 | 0.030      | 0.045    | case 3  |
| $K_s$      | -2.140 | 0.075      | -1.827 | 0.023      | 0.103    | case 1  |
|            | -2.225 | 0.089      | -1.836 | 0.024      | 0.049    | case 2  |
|            | -2.251 | 0.212      | -1.840 | 0.031      | 0.054    | case 3  |
| $W_{JK_s}$ | -2.293 | 0.079      | -2.046 | 0.022      | 0.120    | case 1  |
|            | -2.399 | 0.095      | -2.057 | 0.022      | 0.059    | case 2  |
|            | -2.501 | 0.195      | -2.068 | 0.026      | 0.059    | case 3  |

**Note.** Case 1 is fitted with W Virginis star, case 2 is fitted without W Virginis star, and case 3 is fitted using BL Her stars solely.

using G21, while without ZPO they are about 0.08 mag smaller than with ZPO from L21. The influence of using different ZPO is better visible when applying the determined PLRs for the LMC distance measurement. Column 7 of Table 10 contains measurements of the distance modulus of the LMC determined using each PLR. The distance modulus obtained without introducing ZPO is  $\sim 0.08$  mag higher than with L21 correction and much higher than the reference 18.477 mag value from

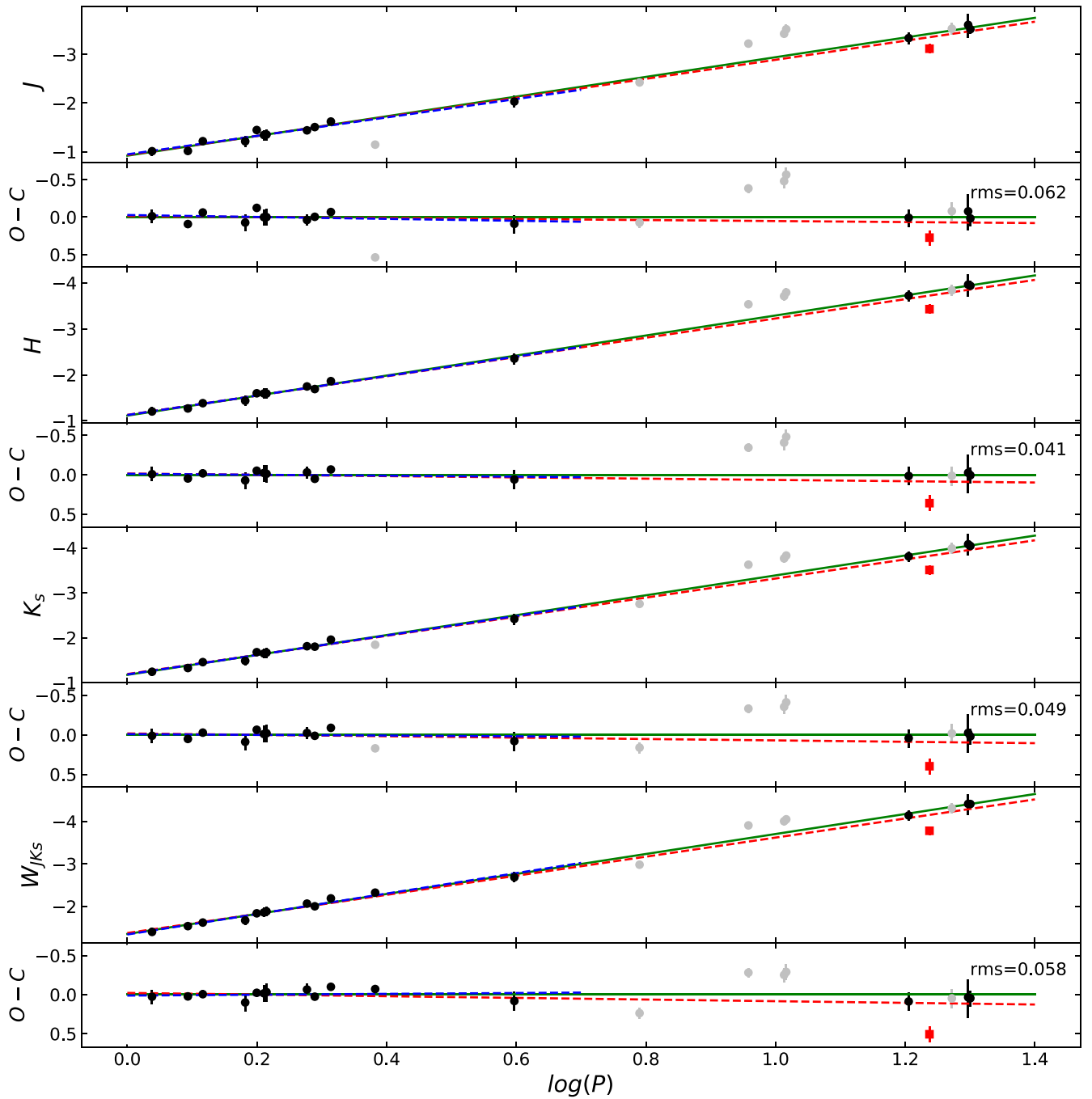


**Figure 15.** Absolute mean magnitudes of Milky Way T2Ceps in  $J$ ,  $H$ , and  $K_s$  and  $W_{JKs}$  wesheit index plotted against logarithm of periods. Black and gray points mark stars used and excluded from fitting procedure, respectively. The red square is W Virginis star, and the red line represent fit including this star, while the green line is obtained excluding it. The blue line is obtained based on BL Her type stars solely. O-C plots present deviations from respective green lines.

eclipsing binaries. G21 corrections give  $\mu$  values lower by  $\sim 0.08$  mag than L21 and also lower than the reference value.

In our calibrations of PLRs for T2Ceps in the MW, we used the ABL approach. It might be interesting to see the difference between ABL and a linear regression fit. We repeat fitting in 10,000 Monte Carlo simulations, but this time we draw magnitudes in a given band and parallaxes from their respective distributions, and using parallaxes we calculate the distance moduli and finally the absolute magnitudes of T2Ceps. Then we fit a straight line (Equation 2,  $\log P_0 = 0.3$ ) using the least squares method. Results of this fitting (for case 2 only, i.e.,

without W Vir star) are also presented in Table 9 (L.R.). The difference between PLRs obtained with ABL and linear regression is not significant (both slopes and intercepts agree within  $1\sigma$ ), and the determined distance modulus of the LMC is almost identical.

In Table 11, we summarize systematic errors on zero-points of PLRs determined for the MW and LMC samples. These values are discussed in Section 2.  $\sigma_{\text{tot}}$  is the total systematic uncertainty (quadratic sum). The main sources of uncertainty in both the MW and the LMC are the distances of T2Ceps (Gaia parallaxes and the LMC distance from Pietrzyński et al. 2019).

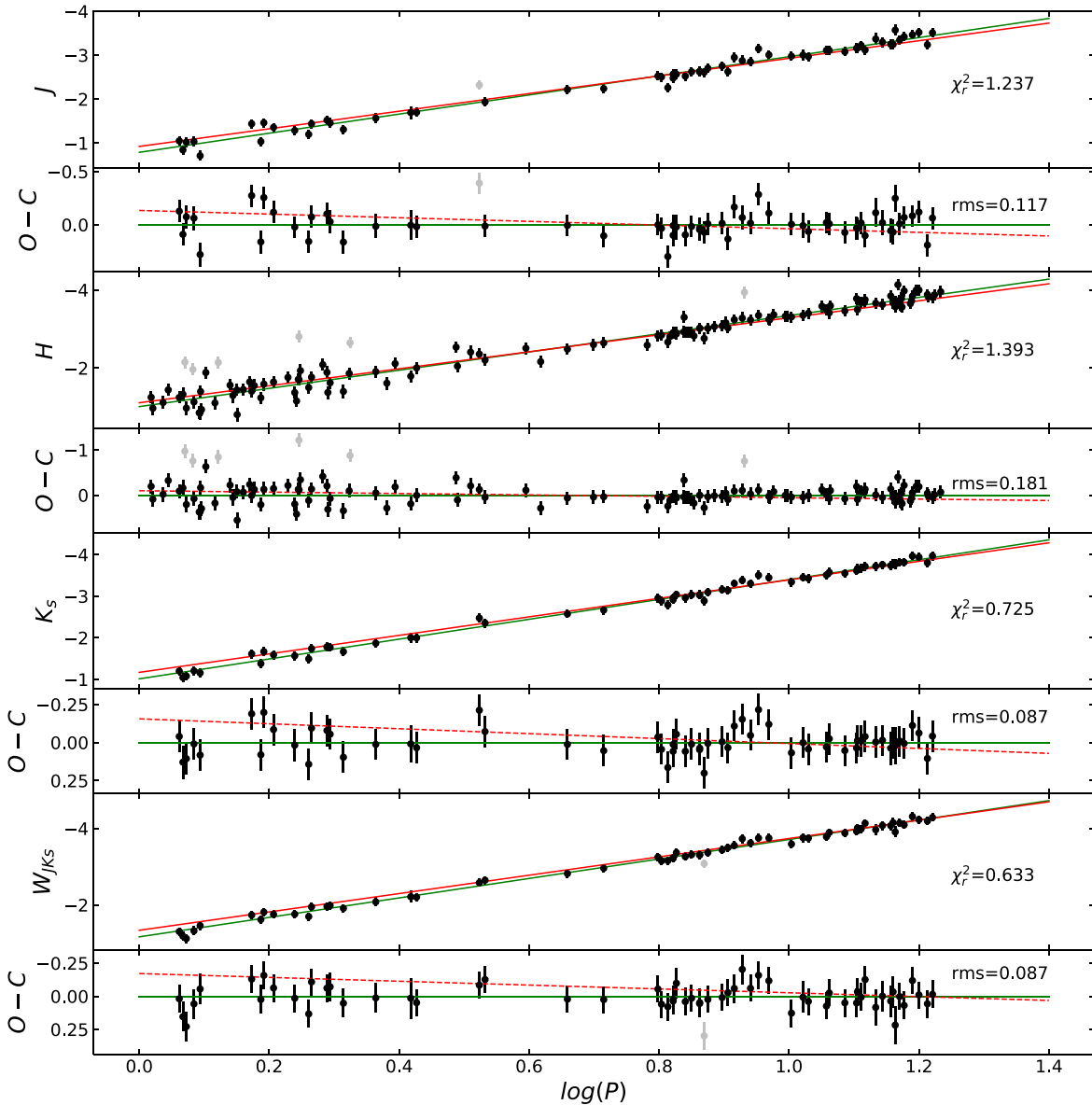


**Figure 16.** Period–luminosity relations of T2Ceps in the Large Magellanic Cloud in  $J$ ,  $H$ ,  $K_s$ , and  $W_{JKs}$  Wesenheit index. Black and gray points mark stars used and excluded from the fitting procedure after  $3\sigma$  clipping applied twice. Green lines are a free fit, and the red dashed lines are PLRs obtained for MW T2Ceps (Table 4).

#### 4.2. The LMC Distance

In column 8 of Table 5, we give statistical errors of our LMC distance modulus measurements, and Table 11 presents sources of systematic uncertainty on both MW and LMC sample. Systematic uncertainty on the LMC distance modulus in each band is quadratic sum of  $\sigma_{\text{tot}}$  for the MW sample and  $\sigma_{\text{phot}}$  and  $\sigma_{\text{redd}}$  for the LMC sample. It gives us the following values. For  $J$  and  $K_s$  bands, we obtain 0.038 mag, 0.060 mag for  $H$  band, and 0.034 mag for  $W_{JKs}$  Wesenheit index. We emphasize that these values are most probably underestimated as we do not take into account the effect of metallicity in the distance determination. As we describe in Section 4.1, using ZPO for Gaia parallaxes from G21 instead of L21 gives us quite discrepant results; thus the ZPO uncertainty stated by Lindegren et al. (2021a) can be underestimated.

Previous determinations of the LMC distance based on T2Ceps rely on the Hipparcos parallax measurements of 2 stars

( $\kappa$  Pav and VY Pyx) and pulsational parallaxes of  $\kappa$  Pav, V553 Cen and SW Tau (Feast et al. 2008). Excluding pW Vir star  $\kappa$  Pav, the absolute distance scale of T2Ceps was tied to 3 stars only. Using pulsational parallaxes of V553 Cen and SW Tau, Matsunaga et al. (2009) found the LMC distance modulus to be  $18.46 \pm 0.10$  mag. Ripepi et al. (2015) in their Figure 11 show the measurements of the distance modulus of the LMC based on different MW calibrators. They used four stars mentioned above (including  $\kappa$  Pav) in addition to RR Lyrae stars with Hubble Space Telescope parallaxes from Benedict et al. (2011), and from different combinations of these anchors, they obtained a value of about 18.57 mag.

The most accurate distance to the LMC was measured using late-type eclipsing binaries by Pietrzyński et al. (2019), and they obtained the distance modulus of  $18.477 \pm 0.004(\text{stat.}) \pm 0.026(\text{sys.})$  mag. The results obtained in this work using BL Her and W Vir stars agree within  $1\sigma$  with this value. Using BL Her stars solely gives significantly higher results. This may be the result of

**Table 5**  
Period–Luminosity Relations for T2Ceps in the Large Magellanic Cloud

| Filter<br>(1) | $a$<br>(2) | $\sigma_a$<br>(3) | $b@ \log P_0 = 0.3$<br>(4) | $\sigma_b$<br>(5) | $\sigma$<br>(6) | $N$<br>(7) | Comment<br>(8)     |
|---------------|------------|-------------------|----------------------------|-------------------|-----------------|------------|--------------------|
| $J$           | −2.177     | 0.040             | −1.442                     | 0.015             | 0.117           | 61         | BLH+WV             |
|               | −2.356     | 0.259             | −1.479                     | 0.039             | 0.164           | 20         | BLH                |
| $H$           | −2.328     | 0.040             | −1.714                     | 0.016             | 0.181           | 122        | IRSF data, BLH+WV  |
|               | −2.195     | 0.300             | −1.783                     | 0.049             | 0.326           | 54         | IRSF data, BLH     |
|               | −1.906     | 0.069             | −2.120                     | 0.027             | 0.170           | 39         | LMCSS data, BLH+WV |
| $K_s$         | −2.387     | 0.030             | −1.729                     | 0.011             | 0.087           | 62         | BLH+WV             |
|               | −2.616     | 0.165             | −1.751                     | 0.025             | 0.105           | 20         | BLH                |
| $W_{JKs}$     | −2.544     | 0.029             | −1.929                     | 0.011             | 0.087           | 61         | BLH+WV             |
|               | −2.796     | 0.153             | −1.946                     | 0.023             | 0.097           | 20         | BLH                |

**Note.** BLH and WV are BL Her and W Vir type stars, respectively.

**Table 6**  
Results of Fitting PLRs for LMC T2Ceps with Slope Fixed on the Corresponding Value Determined from MW Sample

| Filter<br>(1) | $a$<br>(2) | $b@ \log P_0 = 0.3$<br>(3) | $\sigma_b$<br>(4) | $\sigma$<br>(5) | $N$<br>(6) | $\mu$<br>(7) | $\sigma_\mu$<br>(8) | Comment<br>(9)     |
|---------------|------------|----------------------------|-------------------|-----------------|------------|--------------|---------------------|--------------------|
| $J$           | −2.005     | 16.956                     | 0.017             | 0.132           | 61         | 18.481       | 0.029               | BLH+WV             |
|               | −1.955     | 17.016                     | 0.038             | 0.166           | 20         | 18.536       | 0.048               | BLH                |
| $H$           | −2.173     | 16.703                     | 0.017             | 0.190           | 122        | 18.469       | 0.027               | IRSF data, BLH+WV  |
|               | −2.162     | 16.697                     | 0.044             | 0.320           | 54         | 18.461       | 0.048               | IRSF data, BLH     |
|               | −2.173     | 16.473                     | 0.032             | 0.194           | 39         | 18.237       | 0.039               | LMCSS data, BLH+WV |
| $K_s$         | −2.225     | 16.675                     | 0.013             | 0.105           | 62         | 18.511       | 0.027               | BLH+WV             |
|               | −2.251     | 16.743                     | 0.026             | 0.112           | 20         | 18.583       | 0.040               | BLH                |
| $W_{JKs}$     | −2.399     | 16.483                     | 0.013             | 0.101           | 61         | 18.540       | 0.026               | BLH+WV             |
|               | −2.501     | 16.545                     | 0.023             | 0.101           | 20         | 18.613       | 0.035               | BLH                |

**Note.** BLH and WV are BL Her and W Vir type stars, respectively.

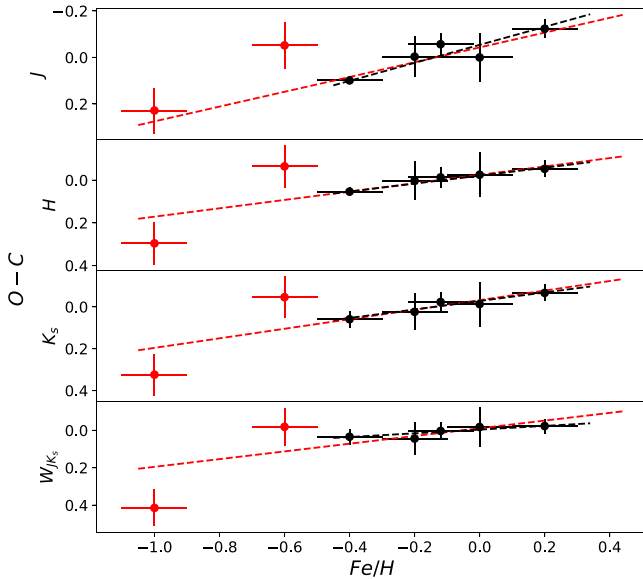


**Figure 17.** Deviation from the period–luminosity relation vs. metallicity for Milky Way T2Ceps. Black points mark BL Her stars, red points are W Vir stars. The red line is the fit for W Vir and BL Her stars, and the black line is for BL Her stars solely.

the metallicity effect and/or a slightly different geometrical distribution of these stars in the LMC compared to eclipsing binaries from Pietrzyński et al. (2019) and W Vir stars, as well as a lower quality of the photometry of these stars in the LMC due to their low brightness and crowding.

**Table 7**  
Estimation of the Metallicity Effect on the Absolute Magnitudes of T2Ceps

| Filter    | $\gamma$ | $\sigma_\gamma$ | Comment |
|-----------|----------|-----------------|---------|
| $J$       | −0.318   | 0.074           | BLH+WV  |
|           | −0.387   | 0.123           | BLH     |
| $H$       | −0.196   | 0.070           | BLH+WV  |
|           | −0.186   | 0.090           | BLH     |
| $K_s$     | −0.228   | 0.076           | BLH+WV  |
|           | −0.203   | 0.111           | BLH     |
| $W_{JKs}$ | −0.181   | 0.076           | BLH+WV  |
|           | −0.107   | 0.101           | BLH     |

**Note.** BLH and WV are BL Her- and W Vir-type stars, respectively.

### 4.3. Metallicity Effect

We investigated the metallicity effect using ZPO from L21; thus we repeat the determination of the  $\gamma$  parameter using G21 ZPO for Gaia parallaxes while not introducing any ZPO, and we obtain almost identical results. Obtained values of the  $\gamma$  parameter are in most cases higher than  $-0.1 \text{ mag dex}^{-1}$  found by Matsunaga et al. (2006), but we can confirm the sign of the effect. It is important to mention that metal abundances of our sample stars are much higher than those in Matsunaga et al. (2006) from GGCs, and that the most metal-poor stars in our sample are two W Vir type stars. Very similar values of  $\gamma$  have been obtained recently empirically for CCeps (Gieren et al. 2018; Breuval et al. 2021; Ripepi et al. 2021). On the other hand, theoretical studies by Das et al. (2021) and Di Criscienzo et al. (2007) yield the metallicity effect for T2Ceps of an opposite sign and actually predict a null effect in the near-

**Table 8**  
Selected Literature Determinations of the Slope of Period–Luminosity Relations for T2Ceps

| Filter     | Host | $a$    | $\sigma_a$ | $\sigma$ | N   | Source | Comment |
|------------|------|--------|------------|----------|-----|--------|---------|
| $J$        | MW   | −2.005 | 0.084      | 0.062    | 14  | TW     | BLH+WV  |
|            | LMC  | −2.177 | 0.040      | 0.164    | 61  | TW     | BLH+WV  |
|            | LMC  | −2.061 | 0.038      | 0.157    | 126 | B17a   | BLH+WV  |
|            | LMC  | −2.190 | 0.040      | 0.130    | 120 | R15    | BLH+WV  |
|            | GB   | −2.240 | 0.031      | 0.316    | 203 | B17b   | BLH+WV  |
|            | GGCs | −2.230 | 0.050      | 0.160    | 46  | M06    | BLH     |
|            |      |        |            |          |     |        | +WV+RVT |
| $H$        | MW   | −2.173 | 0.088      | 0.041    | 14  | TW     | BLH+WV  |
|            | LMC  | −2.328 | 0.040      | 0.181    | 122 | TW     | BLH+WV  |
|            | LMC  | −2.202 | 0.046      | 0.171    | 117 | B17a   | BLH+WV  |
|            | LMC  | −2.316 | 0.043      | 0.200    | 136 | M09    | BLH+WV  |
|            | GB   | −2.591 | 0.163      | 0.353    | 104 | B17b   | BLH     |
|            | GGCs | −2.340 | 0.050      | 0.150    | 46  | M06    | BLH     |
|            |      |        |            |          |     |        | +WV+RVT |
| $K_s$      | MW   | −2.225 | 0.089      | 0.049    | 14  | TW     | BLH+WV  |
|            | LMC  | −2.387 | 0.030      | 0.087    | 62  | TW     | BLH+WV  |
|            | LMC  | −2.232 | 0.037      | 0.180    | 119 | B17a   | BLH+WV  |
|            | LMC  | −2.385 | 0.030      | 0.090    | 120 | R15    | BLH+WV  |
|            | GB   | −2.189 | 0.056      | 0.234    | 201 | B17b   | BLH+WV  |
|            | GGCs | −2.410 | 0.050      | 0.140    | 46  | M06    | BLH     |
|            |      |        |            |          |     |        | +WV+RVT |
| $W_{JK_s}$ | MW   | −2.399 | 0.095      | 0.059    | 15  | TW     | BLH+WV  |
|            | LMC  | −2.544 | 0.029      | 0.087    | 61  | TW     | BLH+WV  |
|            | LMC  | −2.346 | 0.051      | 0.216    | 119 | B17a   | BLH+WV  |
|            | LMC  | −2.520 | 0.030      | 0.085    | 120 | R15    | BLH+WV  |

**Note.** Sources are as follows: TW is this work, B17a (Bhardwaj et al. 2017a), B17b (Bhardwaj et al. 2017b), R15 (Ripepi et al. 2015), M09 (Matsunaga et al. 2009), and M06 (Matsunaga et al. 2006); BLH, WV, and RVT are BL Her, W Vir, and RV Tau type stars, respectively.

**Table 9**  
Parallax Zero-point Offset (ZPO) Determined Using the Procedure from Groenewegen (2021)

| Name         | Gaia ID             | HEALPix level <sup>a</sup> | ZPO<br>(mas)        | $\sigma_{ZPO}$<br>(mas) | ZPO <sub>L21</sub><br>(mas) |
|--------------|---------------------|----------------------------|---------------------|-------------------------|-----------------------------|
| (1)          | (2)                 | (3)                        | (4)                 | (5)                     | (6)                         |
| BX Del       | 1816085861226864768 | 0                          | −0.021              | 0.003                   | −0.0188                     |
| VY Pyx       | 5653136461526964224 | 0                          | −0.033              | 0.003                   | −0.0237                     |
| BL Her       | 4527596850906132352 | 1                          | −0.021              | 0.004                   | 0.0016                      |
| KZ Cen       | 6144045107427693824 | 0                          | −0.011              | 0.003                   | −0.0224                     |
| SW Tau       | 3283721030024735360 | 0                          | −0.038              | 0.007                   | −0.0103                     |
| V971 Aql     | 4188140876549643008 | 0                          | −0.024              | 0.003                   | −0.0175                     |
| DU Ara       | 5814122315506225792 | 2                          | −0.038              | 0.007                   | −0.0189                     |
| V439 Oph     | 4472449191647245184 | 1                          | −0.029              | 0.004                   | −0.0103                     |
| RT TrA       | 5828480459918679936 | 1                          | −0.031              | 0.005                   | −0.0021                     |
| V553 Cen     | 6217308590845895680 | 0                          | −0.017              | 0.003                   | −0.0080                     |
| AU Peg       | 1785352625740690432 | 2                          | −0.028              | 0.005                   | −0.0180                     |
| FM Del       | 1811618408045800832 | 0                          | −0.018              | 0.003                   | −0.0174                     |
| TX Del       | 1734124248699204096 | 0                          | −0.023              | 0.003                   | −0.0112                     |
| $\kappa$ Pav | 6434564460631076864 | 1                          | −0.014 <sup>b</sup> | 0.003                   | 0.0046                      |
| AL Vir       | 6303152720661307648 | 0                          | −0.016              | 0.003                   | −0.0152                     |
| AP Her       | 4510925780739110272 | 1                          | −0.021              | 0.003                   | −0.0028                     |
| CO Pup       | 5643564972301150208 | 0                          | −0.032              | 0.003                   | −0.0212                     |
| W Vir        | 3637042116582796544 | 1                          | −0.026              | 0.003                   | −0.0227                     |
| ST Pup       | 5577329081864722176 | 2                          | −0.035              | 0.003                   | −0.0091                     |
| MR Ara       | 5954403987593491584 | 0                          | −0.027              | 0.003                   | −0.0080                     |
| RS Pav       | 6647640365167706240 | 2                          | −0.030              | 0.006                   | −0.0003                     |
| <b>mean</b>  |                     |                            | <b>−0.026</b>       |                         | <b>−0.013</b>               |

**Notes.** ZPO<sub>L21</sub> is the ZPO from L21 listed for comparison.

<sup>a</sup> HEALPix level defines the resolution of the used ZPO map (for details, see Groenewegen 2021).

<sup>b</sup> Spatial correction only.

**Table 10**

Period–Luminosity Relations for Milky Way T2Ceps Determined Using L21 and G21 Parallax Zero-point Offsets (ZPOs), and without Introducing ZPO (N.A)

| Filter<br>(1) | $a$<br>(2) | $\sigma_a$<br>(3) | $b$<br>(4) | $\sigma_b$<br>(5) | $\sigma$<br>(6) | $\mu$<br>(7) | $\sigma_\mu$<br>(8) | Comment<br>(9) |
|---------------|------------|-------------------|------------|-------------------|-----------------|--------------|---------------------|----------------|
| $J$           | -2.005     | 0.084             | -1.525     | 0.023             | 0.062           | 18.481       | 0.029               | L21            |
|               | -1.917     | 0.079             | -1.485     | 0.023             | 0.059           | 18.401       | 0.030               | G21            |
|               | -2.029     | 0.086             | -1.589     | 0.024             | 0.064           | 18.557       | 0.029               | N.A            |
|               | -2.019     | 0.090             | -1.527     | 0.023             | 0.067           | 18.481       | 0.029               | L.R.           |
| $H$           | -2.173     | 0.088             | -1.757     | 0.022             | 0.041           | 18.469       | 0.027               | L21            |
|               | -2.087     | 0.084             | -1.725     | 0.023             | 0.045           | 18.390       | 0.030               | G21            |
|               | -2.198     | 0.091             | -1.829     | 0.024             | 0.057           | 18.536       | 0.030               | N.A            |
|               | -2.176     | 0.091             | -1.759     | 0.022             | 0.044           | 18.462       | 0.027               | L.R.           |
| $K_s$         | -2.225     | 0.089             | -1.836     | 0.024             | 0.065           | 18.511       | 0.027               | L21            |
|               | -2.137     | 0.084             | -1.796     | 0.023             | 0.045           | 18.431       | 0.028               | G21            |
|               | -2.250     | 0.090             | -1.901     | 0.024             | 0.052           | 18.587       | 0.027               | N.A            |
|               | -2.215     | 0.089             | -1.838     | 0.023             | 0.053           | 18.511       | 0.028               | L.R.           |
| $W_{JKs}$     | -2.399     | 0.095             | -2.057     | 0.022             | 0.061           | 18.540       | 0.026               | L21            |
|               | -2.315     | 0.090             | -2.019     | 0.022             | 0.061           | 18.464       | 0.027               | G21            |
|               | -2.416     | 0.095             | -2.118     | 0.023             | 0.057           | 18.609       | 0.026               | N.A            |
|               | -2.351     | 0.093             | -2.059     | 0.024             | 0.057           | 18.520       | 0.025               | L.R.           |

**Note.** L.R. is the linear regression fit (in 10,000 Monte Carlo simulations) using L21 ZPO.

**Table 11**

Summary of the Estimated Systematic Uncertainties of Zero-points of PLRs for MW and LMC T2Ceps

| Filter    | MW                     |                        |                        |                       | LMC                    |                        |                        |                       |
|-----------|------------------------|------------------------|------------------------|-----------------------|------------------------|------------------------|------------------------|-----------------------|
|           | $\sigma_{\text{phot}}$ | $\sigma_{\text{dist}}$ | $\sigma_{\text{redd}}$ | $\sigma_{\text{tot}}$ | $\sigma_{\text{phot}}$ | $\sigma_{\text{dist}}$ | $\sigma_{\text{redd}}$ | $\sigma_{\text{tot}}$ |
| $J$       | 0.002                  | 0.024                  | 0.02                   | <b>0.031</b>          | 0.02                   | 0.026                  | 0.01                   | <b>0.034</b>          |
| $H$       | 0.002                  | 0.024                  | 0.02                   | <b>0.031</b>          | 0.05                   | 0.026                  | 0.01                   | <b>0.057</b>          |
| $K_s$     | 0.002                  | 0.024                  | 0.01                   | <b>0.026</b>          | 0.02                   | 0.026                  | 0.01                   | <b>0.034</b>          |
| $W_{JKs}$ | 0.003                  | 0.024                  | 0.01                   | <b>0.026</b>          | 0.03                   | 0.026                  | 0.01                   | <b>0.041</b>          |

**Notes.**  $\sigma_{\text{phot}}$  is the photometric zero-point uncertainty;  $\sigma_{\text{dist}}$  is the distance error;  $\sigma_{\text{redd}}$  is the reddening error;  $\sigma_{\text{tot}}$  is total systematic uncertainty (quadratic sum).

infrared regime. The metallicity effect having an opposite sign is also observed for RR Lyrae stars (e.g., Nemec et al. 1994; Neeley et al. 2019). Determining metal abundances for the whole sample of the field T2Ceps in a homogeneous way using high-resolution spectra is crucial for a more precise investigation of the metallicity effect.

### 5. Summary and Conclusions

Using new photometric data and Gaia EDR3 parallaxes of the field T2Ceps, we determined the most precise PLRs for these radially pulsating stars in the near-infrared  $J$ ,  $H$ ,  $K_s$  bands, and  $W_{JK}$  Wesenheit index. We redetermine T2Cep PLRs in the LMC using archival photometry and the most precise distance to this galaxy from eclipsing binaries. Slopes of the obtained MW and LMC PLRs, as well as PLRs for GGCs and GB from the literature, agree at  $2\sigma$  level. We used the obtained MW PLRs to measure the distance modulus of the LMC, and our result in the Wesenheit index  $W_{JKs}$  is  $18.540 \pm 0.026(\text{stat.}) \pm 0.034(\text{syst.}) \text{ mag}$ . Using literature values of metal abundances available for a fraction of field T2Ceps, we investigated the metallicity effect and find it to be of the order of  $-0.2 \text{ mag dex}^{-1}$ , in agreement with the value obtained from studies of T2Ceps in GGCs.

In Figure 18, we present a period–luminosity diagram for LMC T2Ceps, CCeps and Anomalous Cepheids, and nearby pulsating stars not used in this study but classified as T2Ceps in the literature, which are located well on the PLR determined by the LMC sample (and visible from OCA). We plan to collect

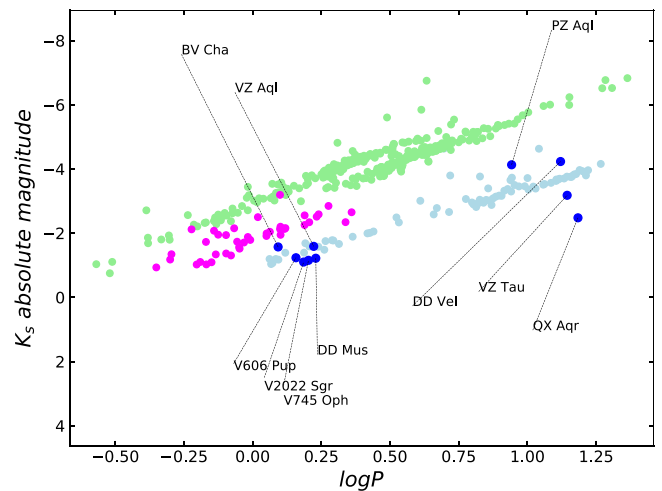


**Figure 18.** The  $K_s$  band period–luminosity diagram for nearby stars cataloged as T2Ceps and not used in this study (blue points) based on the 2MASS photometry. Absolute magnitudes are calculated from Gaia EDR3 parallaxes. The LMC T2Ceps (cyan), CCeps (green), and Anomalous Cepheids (magenta) from the VMC catalog are plotted for comparison.

near-infrared photometry for these stars in the future to increase the precision of fiducial PLRs. Multiband analysis would also benefit from observations in additional passbands; thus we plan to observe these stars in the optical regime. As we mentioned

before, the precise determination of the metallicity effect for T2Ceps requires homogeneous metal abundances for the whole analyzed sample; thus we have started to collect a high-resolution spectra with this end in view.

The main source of systematic error on our PLRs and the LMC distance determination is the Gaia parallax zero-point. We believe that future investigations into this parameter will significantly improve precision and accuracy of PLRs calibrations as well as distance measurements using T2Ceps.

We thank the referee for very valuable comments and suggestions, which helped us to improve the manuscript.

P.W. gratefully acknowledges financial support from the Polish National Science Center grant PRELUDIUM 2018/31/N/ST9/02742. The research leading to these results has received funding from the European Research Council (ERC) under the European Union's Horizon 2020 research and innovation program (grant agreements No. 695099 and No. 951549). Support from DIR/WK/2018/12 grant of the Polish Ministry of Science and Higher Education and the Polish National Science Center grants MAESTRO 2017/26/A/ST9/00446 and BEETHOVEN 2018/31/G/ST9/03050 is also acknowledged. W.G. and G.P. gratefully acknowledge financial support for this work from the BASAL Centro de Astrofísica y Tecnologías Afines (CATA) AFB-170002. B.P. gratefully acknowledges support from the Polish National Science Center grant SONATA BIS 2020/38/E/ST9/00486. R.S. gratefully acknowledges support from the Polish National Science Center grant SONATA BIS 2018/30/E/ST9/00598. A.G. acknowledges support from the ALMA-ANID fund No. ASTRO20-0059. F.P. gratefully acknowledges the generous and invaluable support of the Klaus Tschira Foundation.

Based on data collected under the ESO/CAMK PAN—USB agreement at the ESO Paranal Observatory.

This work has made use of data from the European Space Agency (ESA) mission Gaia (<https://www.cosmos.esa.int/gaia>), processed by the Gaia Data Processing and Analysis Consortium (DPAC, <https://www.cosmos.esa.int/web/gaia/dpac/consortium>). Funding for the DPAC has been provided by national institutions, in particular the institutions participating in the Gaia Multilateral Agreement.

This publication makes use of data products from the Two Micron All Sky Survey, which is a joint project of the University of Massachusetts and the Infrared Processing and Analysis Center/California Institute of Technology, funded by the National Aeronautics and Space Administration and the National Science Foundation. This research has made use of the SIMBAD database, operated at Centre de Données astronomiques de Strasbourg, France (Wenger et al. 2000). We acknowledge with thanks the variable star observations from the AAVSO International Database contributed by observers worldwide and used in this research.

We also thank our colleagues: Miguel Murphy, Marcin Gładkowski, Susanne Blex, Simon Borgniet, Zohreh Ghaffari, Behnam Ghazinouri, Vincent Hocde, Timofej Lisow, Michael Ramolla, Fabian Symietz, and Boris Trahin for their great help in observing in Observatorio Cerro Armazones.

*Software:* gaiadr3\_zero-point (Lindegren et al. 2021a), Astropy7 (Astropy Collaboration et al. 2013, 2018), fnpeaks (<http://helas.astro.uni.wroc.pl/deliverables.php?active=fnpeaks>), IRAF (Tody 1986, 1993), SExtractor (Bertin & Arnouts 1996), SCAMP (Bertin 2006), SWARP (Bertin 2010), DAOPHOT

(Stetson 1987), NumPy (van der Walt et al. 2011; Harris et al. 2020), SciPy (Virtanen et al. 2020), Matplotlib (Hunter 2007).

## ORCID iDs

Piotr Wielgórski  <https://orcid.org/0000-0002-1662-5756>  
 Grzegorz Pietrzyński  <https://orcid.org/0000-0002-9443-4138>  
 Bogumił Pilecki  <https://orcid.org/0000-0003-3861-8124>  
 Wolfgang Gieren  <https://orcid.org/0000-0003-1405-9954>  
 Bartłomiej Zgirski  <https://orcid.org/0000-0003-1515-6107>  
 Marek Górski  <https://orcid.org/0000-0002-3125-9088>  
 Gergely Hajdu  <https://orcid.org/0000-0003-0594-9138>  
 Weronika Narloch  <https://orcid.org/0000-0003-2335-2060>  
 Paulina Karczmarek  <https://orcid.org/0000-0002-0136-0046>  
 Radosław Smolec  <https://orcid.org/0000-0001-7217-4884>  
 Pierre Kervella  <https://orcid.org/0000-0003-0626-1749>  
 Jesper Storm  <https://orcid.org/0000-0002-8627-6096>  
 Alexandre Gallenne  <https://orcid.org/0000-0001-7853-4094>  
 Louise Breuval  <https://orcid.org/0000-0003-3889-7709>  
 Megan Lewis  <https://orcid.org/0000-0002-8069-8060>  
 Mikołaj Kałużczyński  <https://orcid.org/0000-0003-0109-5833>  
 Dariusz Graczyk  <https://orcid.org/0000-0002-7355-9775>  
 Wojciech Pych  <https://orcid.org/0000-0002-7071-598X>  
 Ksenia Suchomska  <https://orcid.org/0000-0001-6118-5844>  
 Mónica Taormina  <https://orcid.org/0000-0002-1560-8620>  
 Gonzalo Rojas Garcia  <https://orcid.org/0000-0001-9266-3036>  
 Rolf Chini  <https://orcid.org/0000-0002-7538-3072>  
 Francisco Pozo Núñez  <https://orcid.org/0000-0002-6716-4179>  
 Catalina Sobrino Figaredo  <https://orcid.org/0000-0001-9704-690X>  
 Martin Haas  <https://orcid.org/0000-0002-7284-0477>  
 Klaus Hodapp  <https://orcid.org/0000-0003-0786-2140>  
 Przemysław Mikołajczyk  <https://orcid.org/0000-0001-8916-8050>  
 Krzysztof Kotysz  <https://orcid.org/0000-0003-4960-7463>  
 Dawid Moździerski  <https://orcid.org/0000-0002-3861-9031>  
 Piotr Kołaczek-Szymański  <https://orcid.org/0000-0003-2244-1512>

## References

- Alcock, C., Allsman, R. A., Alves, D. R., et al. 1998, *AJ*, **115**, 1921  
 Arenou, F., & Luri, X. 1999, in ASP Conf. Ser. 167, Harmonizing Cosmic Distance Scales in a Post-HIPPARCOS Era, ed. D. Egret & A. Heck (San Francisco, CA: ASP), 13  
 Astropy Collaboration, Price-Whelan, A. M., Sipőcz, B. M., et al. 2018, *AJ*, **156**, 123  
 Astropy Collaboration, Robitaille, T. P., Tollerud, E. J., et al. 2013, *A&A*, **558**, A33  
 Baade, W. 1944, *ApJ*, **100**, 137  
 Baade, W. 1958, *AJ*, **63**, 207  
 Balog, Z., Vinko, J., & Kaszas, G. 1997, *AJ*, **113**, 1833  
 Beaton, R. L., Bono, G., Braga, V. F., et al. 2018, *SSRv*, **214**, 113  
 Benedict, G. F., McArthur, B. E., Feast, M. W., et al. 2011, *AJ*, **142**, 187  
 Berdnikov, L. N. 2008, *yCat*, **II/285**  
 Bertin, E. 2006, in ASP Conf. Ser. 351, Astronomical Data Analysis Software and Systems XV, ed. C. Gabriel et al. (San Francisco, CA: ASP), 112  
 Bertin, E. 2010, SWarp: Resampling and Co-adding FITS Images Together, Astrophysics Source Code Library, ascl:1010.068  
 Bertin, E., & Arnouts, S. 1996, *A&AS*, **117**, 393  
 Bhardwaj, A. 2020, *JApA*, **41**, 23  
 Bhardwaj, A., Macri, L. M., Rejkuba, M., et al. 2017a, *AJ*, **153**, 154  
 Bhardwaj, A., Rejkuba, M., Minniti, D., et al. 2017b, *A&A*, **605**, A100  
 Bono, G., Caputo, F., & Santolamazza, P. 1997, *A&A*, **317**, 171  
 Braga, V. F., Bhardwaj, A., Contreras Ramos, R., et al. 2018, *A&A*, **619**, A51  
 Breifelder, J., Kervella, P., Mérand, A., et al. 2015, *A&A*, **576**, A64  
 Breuval, L., Kervella, P., Wielgórski, P., et al. 2021, *ApJ*, **913**, 38  
 Cardelli, J. A., Clayton, G. C., & Mathis, J. S. 1989, *ApJ*, **345**, 245

- Ciechanowska, A., Pietrzyński, G., Szweczyk, O., Gieren, W., & Soszyński, I. 2010, *AcA*, **60**, 233
- Cusano, F., Moretti, M. I., Clementini, G., et al. 2021, *MNRAS*, **504**, 1
- Das, S., Kanbur, S. M., Smolec, R., et al. 2021, *MNRAS*, **501**, 875
- Di Criscienzo, M., Caputo, F., Marconi, M., & Cassisi, S. 2007, *A&A*, **471**, 893
- Drimmel, R., & Spergel, D. N. 2001, *ApJ*, **556**, 181
- Feast, M. W., & Catchpole, R. M. 1997, *MNRAS*, **286**, L1
- Feast, M. W., Laney, C. D., Kinman, T. D., van Leeuwen, F., & Whitelock, P. A. 2008, *MNRAS*, **386**, 2115
- Gaia Collaboration 2020, *yCat*, **I/350**
- Gaia Collaboration, Prusti, T., de Bruijne, J. H. J., et al. 2016, *A&A*, **595**, A1
- Gieren, W., Pietrzyński, G., Soszyński, I., et al. 2005, *ApJ*, **628**, 695
- Gieren, W., Storm, J., Konorski, P., et al. 2018, *A&A*, **620**, A99
- Gingold, R. A. 1985, *MmSAI*, **56**, 169
- Górski, M., Zgierski, B., Pietrzyński, G., et al. 2020, *ApJ*, **889**, 179
- Groenewegen, M. A. T. 2021, *A&A*, **654**, A20
- Groenewegen, M. A. T., & Jurkovic, M. I. 2017, *A&A*, **603**, A70
- Harris, C. R., Millman, K. J., van der Walt, S. J., et al. 2020, *Natur*, **585**, 357
- Harris, H. C., Olszewski, E. W., & Wallerstein, G. 1984, *AJ*, **89**, 119
- Harris, H. C., & Welch, D. L. 1989, *AJ*, **98**, 981
- Hodapp, K. W., Chini, R., Reipurth, B., et al. 2010, *Proc. SPIE*, **7735**, 77351A
- Hunter, J. D. 2007, *CSE*, **9**, 90
- Iwanek, P., Soszyński, I., Skowron, D., et al. 2018, *AcA*, **68**, 213
- Jacyszyn-Dobrzyniecka, A. M., Skowron, D. M., Mróz, P., et al. 2017, *AcA*, **67**, 1
- Jurkovic, M., Szabados, L., Vinkó, J., & Csák, B. 2007, *AN*, **328**, 837
- Kato, D., Nagashima, C., Nagayama, T., et al. 2007, *PASJ*, **59**, 615
- Kochanek, C. S., Shappee, B. J., Stanek, K. Z., et al. 2017, *PASP*, **129**, 104502
- Koen, C., Marang, F., Kilkenny, D., & Jacobs, C. 2007, *MNRAS*, **380**, 1433
- Kovtyukh, V. V., Wallerstein, G., Andrievsky, S. M., et al. 2011, *A&A*, **526**, A116
- Leavitt, H. S. 1908, *AnHar*, **60**, 87
- Lindgren, L., Bastian, U., Biermann, M., et al. 2021a, *A&A*, **649**, A4
- Lindgren, L., Klioner, S. A., Hernández, J., et al. 2021b, *A&A*, **649**, A2
- Lutz, T. E., & Kelker, D. H. 1973, *PASP*, **85**, 573
- Maas, T., Giridhar, S., & Lambert, D. L. 2007, *ApJ*, **666**, 378
- Madore, B. F. 1982, *ApJ*, **253**, 575
- Majaess, D., Turner, D., & Lane, D. 2009, *AcA*, **59**, 403
- Matsunaga, N., Feast, M. W., & Menzies, J. W. 2009, *MNRAS*, **397**, 933
- Matsunaga, N., Feast, M. W., & Soszyński, I. 2011, *MNRAS*, **413**, 223
- Matsunaga, N., Fukushi, H., Nakada, Y., et al. 2006, *MNRAS*, **370**, 1979
- Moskalik, P., & Buchler, J. R. 1990, *ApJ*, **355**, 590
- Neeley, J. R., Marengo, M., Freedman, W. L., et al. 2019, *MNRAS*, **490**, 4254
- Neilson, H. R., Percy, J. R., & Smith, H. A. 2016, *JAVSO*, **44**, 179
- Nemec, J. M., Nemec, A. F. L., & Lutz, T. E. 1994, *AJ*, **108**, 222
- O'Donnell, J. E. 1994, *ApJ*, **422**, 158
- Pietrzyński, G., Gieren, W., Fouqué, P., & Pont, F. 2002, *AJ*, **123**, 789
- Pietrzyński, G., Graczyk, D., Gallenne, A., et al. 2019, *Natur*, **567**, 200
- Pietrzyński, G., Thompson, I. B., Gieren, W., et al. 2012, *Natur*, **484**, 75
- Pilecki, B., Derviřođlu, A., Gieren, W., et al. 2018, *ApJ*, **868**, 30
- Pilecki, B., Gieren, W., Smolec, R., et al. 2017, *ApJ*, **842**, 110
- Plachy, E., Molnár, L., Jurkovic, M. I., et al. 2017, *MNRAS*, **465**, 173
- Pojmanski, G. 2002, *AcA*, **52**, 397
- Rabidoux, K., Smith, H. A., Pritzl, B. J., et al. 2010, *AJ*, **139**, 2300
- Ramolla, M., Westhues, C., Hackstein, M., et al. 2016, *Proc. SPIE*, **9911**, 99112M
- Riess, A. G., Casertano, S., Yuan, W., et al. 2021, *ApJL*, **908**, L6
- Ripepi, V., Catanzaro, G., Molinaro, R., et al. 2021, *MNRAS*, **508**, 4047
- Ripepi, V., Molinaro, R., Musella, I., et al. 2019, *A&A*, **625**, A14
- Ripepi, V., Moretti, M. I., Marconi, M., et al. 2015, *MNRAS*, **446**, 3034
- Schlafly, E. F., & Finkbeiner, D. P. 2011, *ApJ*, **737**, 103
- Skrutskie, M. F., Cutri, R. M., Stiening, R., et al. 2006, *AJ*, **131**, 1163
- Smolec, R. 2016, *MNRAS*, **456**, 3475
- Smolec, R., Moskalik, P., Plachy, E., Soszyński, I., & Udalski, A. 2018, *MNRAS*, **481**, 3724
- Soszyński, I., Smolec, R., Udalski, A., & Pietrukowicz, P. 2019, *ApJ*, **873**, 43
- Soszyński, I., Udalski, A., Pietrukowicz, P., et al. 2011, *AcA*, **61**, 285
- Soszyński, I., Udalski, A., Szymański, M. K., et al. 2008, *AcA*, **58**, 293
- Soszyński, I., Udalski, A., Szymański, M. K., et al. 2017a, *AcA*, **67**, 103
- Soszyński, I., Udalski, A., Szymański, M. K., et al. 2017b, *AcA*, **67**, 297
- Soszyński, I., Udalski, A., Szymański, M. K., et al. 2018, *AcA*, **68**, 89
- Stetson, P. B. 1987, *PASP*, **99**, 191
- Suchomska, K., Graczyk, D., Smolec, R., et al. 2015, *MNRAS*, **451**, 651
- Templeton, M. R., & Henden, A. A. 2007, *AJ*, **134**, 1999
- Tody, D. 1986, *Proc. SPIE*, **627**, 733
- Tody, D. 1993, in *ASP Conf. Ser. 52, Astronomical Data Analysis Software and Systems II*, ed. R. J. Hanisch, R. J. V. Brissenden, & J. Barnes (San Francisco, CA: ASP), 173
- van der Marel, R. P., & Cioni, M.-R. L. 2001, *AJ*, **122**, 1807
- van der Walt, S., Colbert, S. C., & Varoquaux, G. 2011, *CSE*, **13**, 22
- Virtanen, P., Gommers, R., Oliphant, T. E., et al. 2020, *NatMe*, **17**, 261
- Wallerstein, G. 2002, *PASP*, **114**, 689
- Watermann, R. 2012, PhD thesis, Astronomisches Institut Ruhr-Universitaet Bochum, <https://hss-opus.ub.ruhr-uni-bochum.de/opus4/frontdoor/index/index/year/2019/docId/3005>
- Wenger, M., Ochsenbein, F., Egret, D., et al. 2000, *A&AS*, **143**, 9